Article

The Passa Três Granite Intrusion-Related/Hosted Neoproterozoic Gold Deposit (Paraná State, Brazil): Mineralogical, Geochemical, Fluid Inclusion and Sulphur Isotope Constraints

Bárbara Carolina Dressel [1,2,3], Alain Chauvet [1,*], Kalin Kouzmanov [4], Barbara Trzaskos [2], Olivier Bruguier [1], Patrick Monié [1], Sandro Notto Villanova [5] and José Bazille Newton [5]

[1] Géosciences Montpellier, Université de Montpellier, CNRS, 34095 Montpellier, France; barbara.c.dressel@gmail.com (B.C.D.); olivier.bruguier@umontpellier.fr (O.B.); patrick.monie@umontpellier.fr (P.M.)

[2] Post-Graduation Program in Geology, Geology Department, Federal University of Paraná, Av. Coronel Francisco Heráclito dos Santos, 210, Curitiba 81531-970, PR, Brazil; barbaratrzaskos@ufpr.br

[3] Capes-PDSE Scholarship Process n. 99999.006489/2015-00, CAPES Foundation, Ministry of Education of Brazil, Brasília 70040-020, DF, Brazil

[4] Department of Earth Sciences, University of Geneva, Rue des Maraîchers 13, 1205 Geneva, Switzerland; kalin.kouzmanov@unige.ch

[5] Mineração Tabiporã, Rua Maria Aparecida de Oliveira, 803-Lt. São Gerônimo, Campo Largo 83606-177, PR, Brazil; sn.villanova@gmail.com (S.N.V.); josebazille@hotmail.com (J.B.N.)

[*] Correspondence: alain.chauvet1@umontpellier.fr

Abstract: The Passa Três granite is a 5 km^2 intrusion in southern Brazil with an NNE–SSW-elongated shape, hosting gold-bearing quartz veins with fluorite, carbonates, sulphides (pyrite, chalcopyrite, aikinite, molybdenite) and native gold. Orebodies are hosted by the pluton roof zone, which is marked by various textures indicating magmatic–hydrothermal transition processes. Mineralisation formed between 613 and 608 Ma in extensional pull-apart structures controlled by two conjugated N–S and E–W fault systems. We report results from petrography, quantitative evaluation of minerals by scanning electron microscopy (QEMSCAN), scanning electron microscopy (SEM), electron probe microanalyses (EPMA), X-ray fluorescence (XRF), trace element analyses of pyrite by laser ablation inductively coupled plasma mass spectrometry (LA-ICP-MS), sulphur isotope (δ^{34}S) analyses, and fluid inclusion microthermometry. Hydrothermal alteration is dominantly developed as phengite–quartz–carbonate and sericite–carbonate–chlorite assemblages along mineralised structures. Fluid inclusion study indicates mineralising fluids with H$_2$O-CO$_2$-NaCl composition, low to moderate salinity (0.2–12.84 wt % NaCl eq.), and temperatures from 400 to 150 °C. The sulphur isotopic composition of pyrite (−0.1 to 1.1‰) suggests magmatic origin. These data, in conjunction with structurally controlled mineralisation enriched in Au-Bi minerals shortly post-dating the granite emplacement, appoint towards similarities between the Passa Três deposit and intrusion-related gold systems. The specific location of the mineralisation in the core (and in the roof zone, regarding its vertical position) of the Passa Três granitic intrusion defines it as "granite-hosted" thus, it is representative of a specific model that can be used for exploration of other intrusion-related/hosted gold deposits near the studied area or in other locations.

Keywords: magmatic–hydrothermal; gold-bearing quartz vein; intrusion-related gold deposit; granite-hosted gold deposit; Passa Três granite; Brazil; Neoproterozoic

1. Introduction

Intrusion-related gold deposits (IRGD) have been defined as a type of mineralisation in which gold frequently occurs in a distal or proximal position with respect to the

causative magmatic body as gold-bearing quartz veins emplaced within the surrounding rocks or hosted in the magmatic body itself [1–5]. The main characteristics of IRGD include: (i) spatial/temporal association between magmatism and ore formation; (ii) spatial association of gold-bearing ore bodies with cupolas of reduced granitic plutons; (iii) gold in sheeted quartz veins frequently emplaced outward of the intrusion; (iv) significant Bi, W, and Te geochemical anomalies; (v) low-salinity and CO_2-rich mineralising fluids; and (vi) low sulphide content of the ore associated with low-grade gold mineralisation. A complex alteration history with dominant chlorite, sericite, and carbonate stages and a reduced character of the causative intrusion are two additional features [1,6–9].

The Passa Três granite-hosted mineralisation is particular with respect to the above-cited features because the gold-bearing quartz veins are located inside the intrusion itself and are developed under extensional local tectonics, resulting in the generation of multiple normal faults and pull-apart structures, hosting the main orebodies. Orebodies are not sheeted veins at Passa Três granite but consist of metre-scale veins, frequently pull-apart, features only developed along normal faults, with two main trends (N–S and E–W). These orebodies are exploited for gold by the Mineração Tabiporã mining company (specifically the Barreiro zone) since the 1980s, constituting the only active gold mine in the south of Brazil. In the case of the Passa Três gold deposit, mineralisation is located inside the intrusion but in the roof zone, as a typical IRGD model [7–9]: (i) mineralisation is shortly post-dating the granite emplacement; (ii) evidence for magmatic–hydrothermal transition processes in the area hosting the orebodies (presence of unidirectional solidification textures (UST), stockscheider, and abundant quartz-K-feldspar veins); (iii) gold is associated with Bi-minerals; (iv) orebodies are structurally controlled; and (v) mineralisation is hosted by the cupola zone of a small granitic intrusion [10].

Representing an important gold deposit in the State of Paraná, several studies were conducted in order to understand the igneous intrusion, sources of fluids, mineralisation, and hydrothermal alteration, leading to different discussions concerning its model, such as porphyry-type [11–13], "plutogenic" deposit, where the veins disposition was compared to the Riedel system [14,15], and the lode deposit was associated with shear zones [16] and IRGD [10,17]. Other studies focused on its geochemistry [18] and the structural setting and control of the orebodies [19], suggesting that the orebodies were formed after the granite's emplacement and were later affected by three high-angle fault systems. A common point is the assumption that ore fluids transportation and hydrothermal activity are involved within the structures of the Lancinha Shear Zone [11,12,15,16,20–22].

In the light of the ongoing debate regarding the IRGD, syenite-hosted gold deposits, alkaline gold, and the "non-granite-related" alternative for mesothermal gold deposits and deposits associated to shear zones, and specifically those emplaced inside magmatic intrusions, we present complementary mineralogical and geochemical data concerning the Passa Três granite-hosted gold mineralisation in Brazil (also known as the Barreiro zone) in order to confirm its intrusion-related affinity and to propose a new model of intrusion-related/hosted mineralisation. Fluid inclusion characteristics, hydrothermal alteration styles, and new $\delta^{34}S$ isotope data are presented and discussed here aiming to better characterise mineralisation events and to decipher the origin and potential sources of the mineralising fluids.

2. Geological Setting

2.1. Regional Geology

The Eastern Paraná state (Southern Brazil) is composed of four domains presumably amalgamated during the Neoproterozoic, that include, from north to south, the Apiaí, Curitiba, Luís Alves, and Paranaguá terranes (Figure 1A), which are all representative of the southern part of the large-scale Ribeira Mobile Belt [23]. Three main tectonic events affected the Precambrian terranes located in the region (Açungui Thrust System, Apiaí Folding System, and the Lancinha Shear System) (Figure 1A) [24–29]. The Passa Três granitic intrusion is located south of the Apiaí terrane and crops out in the core of the Mesoproterozoic

Votuverava Group composed of a monotonous succession of meta-pelitic rocks (sericite schists, phyllites, slates), with subordinate intercalations of meta-arenites, rare carbonate rocks, and meta-basites [30]. In fact, the southern part of the Apiaí Terrane is supposed to be deformed and affected by a few shearing events, involving the formation of several thrust and strike–slip shear zones [25,30–32]. These events were related to the oblique Neoproterozoic collision between the San Francisco, Congo, and Paraná cratons [33–35] that implies the deformation of the sedimentary sequence under low- to medium-grade metamorphism [31].

Two main episodes of magmatism have been described in the studied area. The first one, from 700 to 600 Ma, reflects the formation of a magmatic arc (Cordilleran type) in response to the closure of the Adamastor Ocean and is linked to an extensive calc-alkaline intrusive magmatism represented by syn- to post-tectonic I-type granites, emplaced between 630 and 600 Ma (i.e., the Cunhaporanga and Três Córregos batholiths [31,36–39]). From 600 Ma onward, the Adamastor Ocean was completely consumed, and most continental blocks were amalgamated (see above), which was followed by the development of dextral shear zones related to ongoing oblique collision and/or escape tectonics (e.g., the above-cited Lancinha Shear System). In this context, pull-apart basins were created, filled by molasse sequences (e.g., Castro Group), and the sedimentary units were intruded by post-tectonic granites during the second magmatic episode between 590 and 560 Ma (A-type magmatism generating the Cerne, Passa Três, Piedade, Morro Grande, and Varginha granitic intrusions—Figure 1A, [31,40]).

2.2. Local Geology

The Passa Três granite is classified as a I-type intrusion due to its metaluminous character (its classification is still controversial in the literature) and its mineralogy marked by the occurrence of magnetite, sphene, apatite, amphibole, and biotite [15]. Classified as shoshonitic and belonging to the magnetite-series granitoids [15,16], this intrusion is considered as post-collisional, similarly to other local intrusions (e.g., Varginha, Morro Grande, Piedade, and Cerne granites) (Figure 1A). Regarding its origin, the Passa Três Granite is considered as hybrid (crustal–mantellic origin), intruded in a late-orogenic or late to post-collisional context, as part of the Três Córregos-Cunhaporanga magmatic arc [11,12,15]. The emplacement of the Passa Três granite is also considered as syn- to late-tectonic regarding the activity of major transcurrent shear zones [41,42]. Additionally, Cury [42] suggested that crustal contamination can significantly affect the magma composition, as indicated by the rare earth element (REE) patterns, and they compared the Passa Três granitic intrusion to the A-type granites, contrasting with the above-mentioned hypothesis.

Three texturally different facies characterise the Passa Três granite—a "medium-grained granite" (GEM, *granite equigranulaire moyen* in French), a "microgranite" (GEF, *granite equigranulaire fin* in French), and a "white granite" (GEB, *granite equigranulaire blanc* in French) (in this study, we adopted the same facies names as used in the mine), in addition to aplites and pegmatites. GEM and GEF are isotropic and they only differ by their texture (medium-grained versus fine-grained). In terms of field relationships, GEF and GEM facies seem contemporaneous and crop out along the whole length of the intrusion. Therefore, hereafter, both will be termed as "red granite" due to the dominantly reddish colour of the rocks. The "white granite" facies is medium-grained and isotropic. It crosscuts the other two facies and has been only seen in drill cores, never in outcrops.
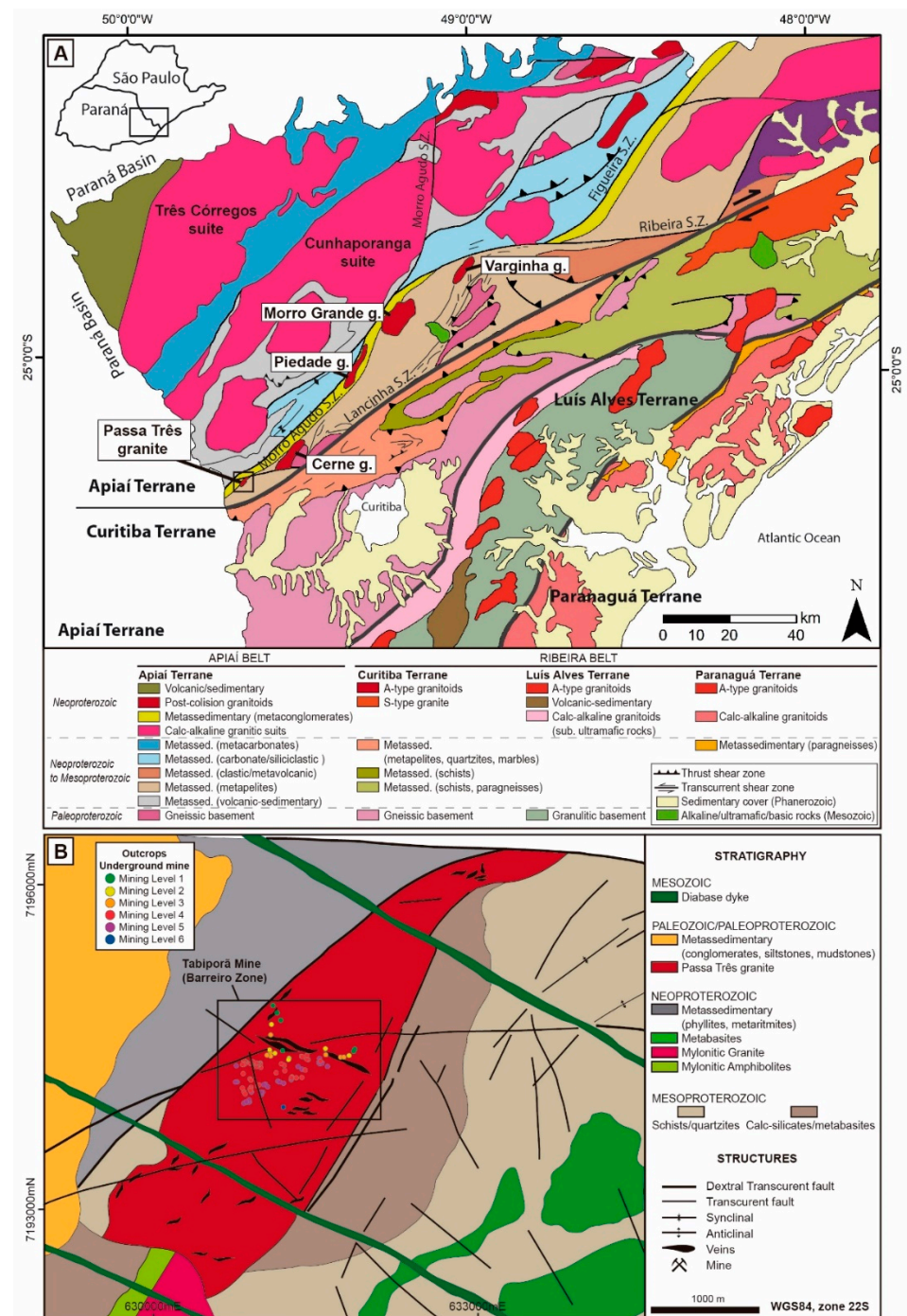
Figure 1. (**A**) Geological map of the Eastern Paraná State with localisation of the Passa Três granite; the Apiaí, Curitiba, Luís Alves, and Paranaguá terranes are also indicated with limits marked by a grey thick line (adapted from [43]); (**B**) Local geological map of Passa Três granite and surrounding rocks (adapted from [15]) with indication of the sample's location by mine level.

The mineralisation associated with this granitic intrusion is represented by metre-scale quartz veins at the Barreiro zone (Figure 1B), with mostly irregular shapes, defining extensional pull-apart structures filled by quartz, sulphides (pyrite, chalcopyrite, aikinite, molybdenite), fluorite, muscovite, sericite, carbonates, and visible gold [10]. Two vein systems, trending E–W and N–S with south and west dipping, respectively, are recognised and thus define two extensional fault systems, which are supposed to be conjugated. The abundance of aplites and pegmatites near the orebodies, the observation of veins with abundant K-feldspar along contacts, and the identification of stockscheider and UST

strongly suggest that the mineralised system could have been formed as a continuum during the magmatic–hydrothermal transition and consists of late-stage magmatic features evolving to hydrothermal ore-bearing veins [10]. Despite the fact that orebodies deformed by these structures were not encountered, this hypothesis was confirmed by U-Pb (zircon) (laser ablation inductively coupled plasma mass spectrometry, LA-ICP-MS) and Ar-Ar (muscovite) geochronology of magmatic and hydrothermal minerals. The red granite facies displays U-Pb zircon ages of 611.9 ± 4.7 Ma (GEM) and 611.9 ± 5.6 Ma (GEF), whereas the white granite facies yields a younger U-Pb zircon age of 592 ± 7 Ma (GEB). Ar-Ar dating on muscovite provides consistent ages from 612 to 608 ± 2 Ma for the quartz–feldspar magmatic–hydrothermal veins and from 611 to 608 ± 2 Ma for the orebodies [10]. Based on these data, we consider the lifetime of the system (from granite crystallisation to mineralised vein emplacement) to be of 5 Ma (bracketed between 613 and 608 Ma), which is itself a strong argument in favour of the genetic link between granitic magmatism, hydrothermal activity, and mineralisation.

Hydrothermal alteration styles associated with the gold mineralisation remain poorly characterised at the Passa Três deposit. Few works have described some alteration mineral occurrences expressed as alteration of biotite/amphibole, K-feldspar alteration, sericite/muscovite alteration, argillic alteration, carbonation, silicification, epidotisation, and saussuritisation [15,16,18,42]. In fact, the large list of alteration styles in the deposit demonstrates that this point needs reconsideration due to a lack of data on mineralising fluid composition and sources.

3. Materials and Methods

The samples from hydrothermally altered rocks and orebodies were collected from different drill holes and various mine workings in the six accessible levels of the underground mine (approximate altitude of the levels: 790 m (mine level 1), 750 m (mine level 2), 690 m (mine level 3), 630 m (mine level 4), 550 m (mine level 5), 480 m (mine level 6); obs.: surface altitude: 850–900 m) (Figure 1B). Polished thin sections were prepared in order to determine the paragenetic relationships of ore minerals and to characterise the various stages of alteration. Electron probe microanalyses (EPMA) and back-scattered electron (BSE) images were acquired on six representative carbon-coated thin sections with a Cameca SX100 Electron Microprobe Microanalyzer by wavelength dispersion spectrometry (WDS) at the University of Montpellier (France). Measurements were done at an accelerating voltage of 20 kV with a beam current of 10 nA and a beam diameter of 1 μm, using the following X-ray lines for silicate and carbonate minerals: F ($K\alpha$), Al ($K\alpha$), Si ($K\alpha$), Ti ($K\alpha$), Na ($K\alpha$), Mg ($K\alpha$), Mn ($K\alpha$), Fe ($K\alpha$), K ($K\alpha$), and Ca ($K\alpha$), and for the metallic minerals: S ($K\alpha$), Fe ($K\alpha$), Cu ($K\alpha$), Au ($L\alpha$), Mo ($L\alpha$), Pb ($M\alpha$), Ag ($L\alpha$), Zn ($K\alpha$), Ti ($K\alpha$), As ($L\alpha$), and Bi ($L\alpha$). For the analysis of sulphides, the following counting times and crystal arrangement were employed: counting times: S, Ti, Zn, As (40 s); Mo, Ag (30 s); Pb, Fe, Cu, Au, Bi (20 s); crystals arrangement: crystal "LPET" (Mo, Pb, Ag), crystal "LLIF" (Fe, Cu, Au, Bi), crystal "PET" (S, Ti), crystal "TAP" (Zn, As). For the analyses of the silicates, the following counting times and crystals arrangement were used during three analysis sessions: (1) counting times: Mg (40 s); Ti, Mn, Fe, K, Ca (30 s); F, Al, Si, Na (20 s); crystals arrangement: crystal "LPET" (K, Ca); crystal "LLIF" (Mn, Fe); crystal "PET" (Ti), crystal "TAP" (F, Al, Si, Na, Mg); (2) Mg (40 s); Al, Si, Ti, K, Ca, Cr (30 s); Mn, Na, Fe, Ni (20 s); crystals arrangement: crystal "LPET" (K, Ca); crystal "LLIF" (Mn, Fe, Ni); crystal "PET" (Ti, Cr); crystal "TAP" (Al, Si, Na, Mg); (3) Mg (40 s); Ti, Cr (30 s); Cl, Ni, Mn, Fe, K, Ca, F, Al, Si, Na (20 s); crystals arrangement: crystal "LPET" (Cl, K, Ca), crystal "LLIF" (Ni, Mn, Fe), crystal "PET" (Ti, Cr), crystal "TAP" (F, Al, Si, Na, Mg). Elements such as Cu, Au, Mo, Pb, Ag, Zn, Ti, As, and Bi were measured in pyrite but are systematically below the limit of detection, and only Fe and S were quantified with EPMA.

X-ray fluorescence (XRF) whole rock lithogeochemistry analyses were performed at the Acme Laboratory (Bureau Veritas Group), Belo Horizonte (Brazil) on five samples.

Scanning electron microscopy (SEM) with energy-dispersive spectroscopy (EDS) analyses were performed using an FEI Quanta 200 FEG with a Silicon Drift X-MaxN detector for EDS analysis, at Géosciences Montpellier, University of Montpellier (France), using the following parameters: accelerating voltage (15 kV), working distance (10 mm), spot size (3.5 μm).

The determination of trace elements for sulphides and gold was performed by LA-ICP-MS. Analyses were conducted at Géosciences Montpellier (AETE-ISO analytical platform of the OSU OREME, University of Montpellier) using an Element XR single collector mass spectrometer coupled to a GEOLAS system housing a Compex 102,193 nm excimer laser. Prior to analyses, the instrument was tuned for maximum sensitivity and low oxide production (ThO/Th < 1%), using an NIST612 glass. This includes torch alignment and gas flow optimisation. Ablation experiments were conducted in a He atmosphere, which enhances sensitivity and reduces inter-element fractionation. Then, the helium gas stream and particles from the samples were mixed with Ar before entering the plasma. Twenty-five points were analysed (pyrite 2a, pyrite 2b, chalcopyrite, aikinite, and native gold) with a spot size of 15 μm, a frequency of 4 Hz, and an energy density of 8 J/cm^2. Each analysis included a surface cleaning of 5 pulses, which was followed by a background acquisition of 90 s and subsequently 40 s of data acquisition of the sample. The polymetallic sulphide MASS1 [44] and the NIST 612 were used as external certified reference materials (values from Georem at http://georem.mpch-mainz.dwdg.de, accessed on 25 October 2016). Monitored isotopes were ^{59}Co, ^{60}Ni, ^{65}Cu, ^{66}Zn, ^{75}As, ^{107}Ag, ^{121}Sb, ^{125}Te, ^{197}Au, ^{208}Pb, and ^{209}Bi with a dwell time of 12 ms. Iron or S was used as the internal standard. Data reduction was carried out with the Glitter software package (http://www.glitter-gemoc.com, accessed on 25 October 2016).

Automated mineral analysis and textural imaging of the studied samples (thin polished sections) were performed using an FEI QEMSCAN® (quantitative evaluation of minerals by scanning electron microscopy) Quanta 650F facility at the Department of Earth Sciences, University of Geneva (Geneva, Switzerland). The system is equipped with two Bruker QUANTAX light-element EDS detectors. Analyses were conducted at high vacuum, accelerating voltage of 25 kV, and a beam current of 10 nA on carbon-coated polished thin sections. Field Image operating mode [45] was used for analyses. In total, 221 individual fields were measured per sample, with 1500 μm per field, and point spacing of 5 μm. The standard 1000 counts per point were acquired, yielding a limit of detection of approximately 2 wt % per element for mineral classifications. Measurements were performed using iMeasure v5.3.2 software and data processing using iDiscover® v5.3.2 software package. Final results consist of: (i) high-quality spatially resolved and fully quantified mineralogical maps; (ii) BSE images with identical resolution as the mineralogical maps; and (iii) qualitative X-ray element distribution maps.

Ten double-polished thick sections (200 μm) were used for fluid inclusion analysis. Microthermometric measurements were carried out using a conventional microscope equipped with a Linkam MSG600G heating/freezing stage with temperature range from –180 °C to +600 °C, with a precision of 0.1 °C, at the Lamir Laboratory, Federal University of Paraná (Curitiba, Brazil). A set of synthetic fluid inclusion standards of pure H_2O and CO_2-H_2O at 50% mol was used for calibration.

Isotope analyses of sulphur were performed at the Actlabs Laboratories at Ancaster (Canada) on five pyrite samples (concentrate pulp) of the main mineralised veins. The samples were analysed by isotope ratio mass spectrometry (Mat 253, Thermo Scientific, IRMS coupled with a Fisons Instruments EA for ^{34}S-SO$_4$ analysis). Dried samples are weighed into tin cups for ^{34}S analysis: approximately 0.3 mg of sample is used for ^{34}S analysis, with 3 mg of niobium pentoxide added to each sample to ensure complete sample combustion at a temperature of 980 °C. Data correction and normalisation are based on three international standards (IAEA SO6, IAEA SO5, and NBS 127) and two calibrated internal standards that bracket the samples. The obtained results present the peak area within acceptable levels and standard deviation within specs (± 0.5‰), according to Actlabs procedures.

4. Results

In this section, results on the red granite and remarks on its red colour are presented as well as the mineral composition of the orebodies and data about the mineral chemistry of the ore minerals, highlighting the Au-Cu-Bi-Pb association.

4.1. Petrology, Texture, and Mineralogy

4.1.1. Red Granite

The red granite is present in all outcrops of the Passa Três granite (Figure 2A,B). Compositionally, the red granite corresponds to a syenogranite and presents an igneous paragenesis composed of microcline, plagioclase, quartz, and biotite and has a medium- to fine-grained texture with isotropic structure. Zircon, fluorite, sphene, and apatite are common accessories. Chlorite (clinochlore in composition, see Section 6) occurs as an alteration product of biotite and possibly amphibole (Figure 2C,D). Magnetite occurs associated with sphalerite, presenting well-formed crystals. Hematite is anhedral and also occurs with magnetite, carbonate, and sericite as alteration aggregates. EPMA analyses also suggest the presence of Fe-dolomite, siderite, and calcite as the main carbonate minerals associated with alteration (see Section 6).

The red colour is homogeneously distributed at the scale of the entire Passa Três granite and is characteristic of the main facies of the pluton. This colour is possibly due to the presence of hematite inclusions within the K-feldspar, as evidenced by SEM imaging and EDS analysis (Figure 2E–G). Hematite inclusions in K-feldspar crystals may form by high-temperature alteration, as suggested by Nakano [46] and Putnis [47]. In this case, the alteration would be older than the mineralisation. Another possibility is the exsolution of Fe_2O_3 due to the formation of crypto- and micro-pertites in the K-feldspar (Supplementary Material A, Figure S1), which can be formed on cooling and/or in the presence of fluids [48]. As the presence of pertites in the K-feldspar from the studied intrusive rock is commonly observed and there is no other evidence of high-temperature alteration, we consider the red granite as the main facies of the Passa Três granite and thus as a pre-hydrothermal alteration feature of the intrusion.
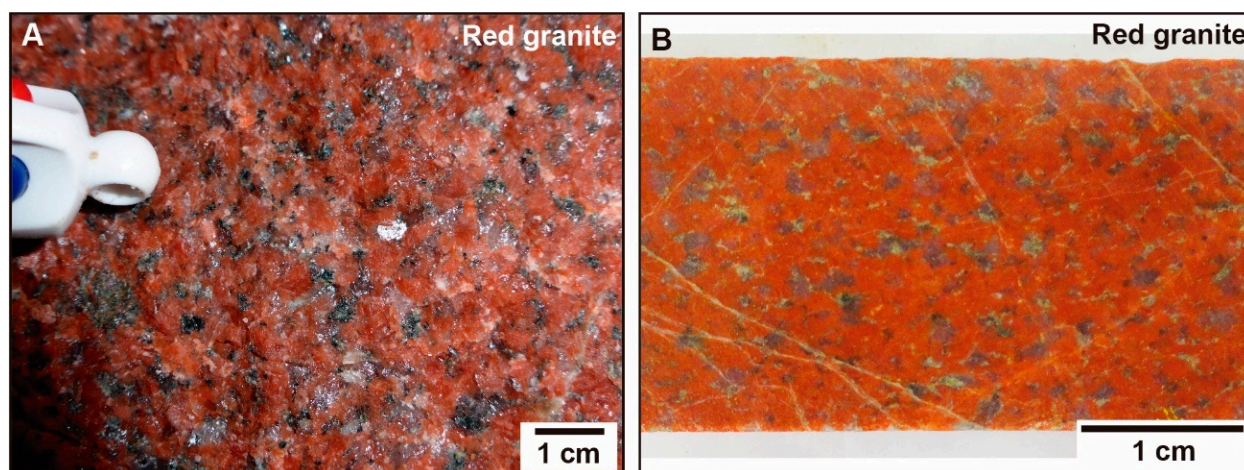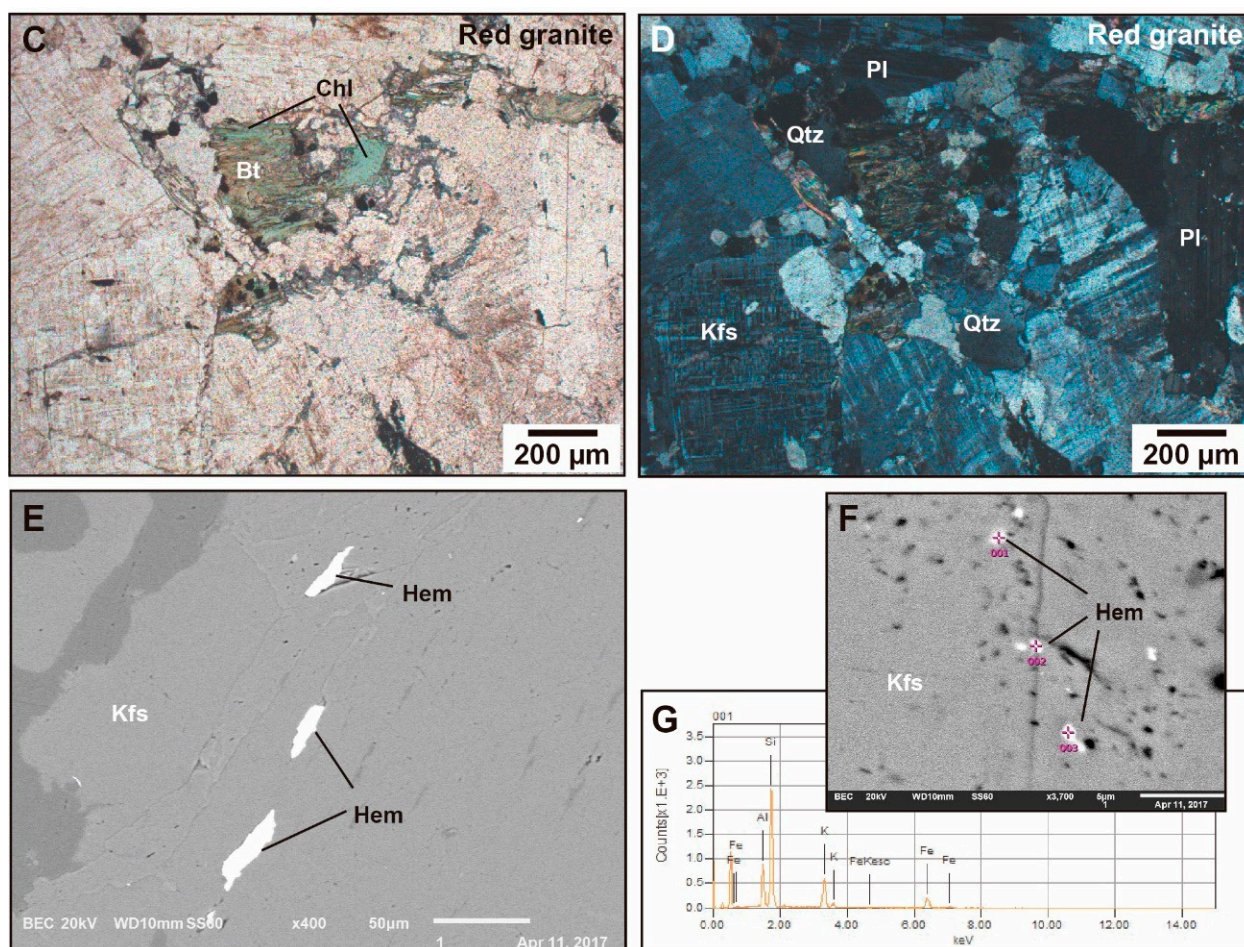

Figure 2. *Cont*.

Figure 2. Red granite textures: (**A**,**B**) Red granite with medium-grained isotropic texture; biotite crystals altered to chlorite; photographs come from underground mine (**A**) and from borehole (**B**); (**C**,**D**) Photomicrographs in natural (**C**) and polarized (**D**) light of the red granite with biotite altered to chlorite, in a medium-grained isotropic texture (thin section of sample from underground mine); (**E**) scanning electron microscopy (SEM)/back-scattered electron (BSE) image showing elongated hematite crystals in planes parallel to the K-feldspar cleavage; (**F**) Hematite crystals in pores of K-feldspar with location of energy-dispersive spectroscopy (EDS) analyses (SEM-BSE image); (**G**) EDS spectrum indicating the presence of Fe in the inclusions analysed. Abbreviations: Bt—biotite; Chl—chlorite; Hem: hematite; Kfs—K-feldspar; Pl—plagioclase; Qtz—quartz.

4.1.2. Gold Mineralisation

Regarding the composition of the orebodies (Figure 3A,B), four stages have been identified: stage 1 (quartz 1 + fluorite); stage 2a (quartz 2 + pyrite 2a ± native gold ± chalcopyrite ± aikinite ± fluorite ± sphalerite ± muscovite); stage 2b (quartz 2 + pyrite 2b + native gold + chalcopyrite + aikinite + Fe-dolomite ± sphalerite ± fluorite ± muscovite); and stage 3 (quartz 3 + Fe-dolomite + calcite + molybdenite + aikinite + muscovite + fluorite) (obs.: minerals numbers correspond to the stage's number, not to order of occurrence) [10]. In this context, gold occurs mainly as native gold grains in fractures that affected pyrite, commonly in association with chalcopyrite and aikinite (Figure 3C–E). Gold distribution is confirmed by SEM images when massive pyrite 2a precedes euhedral pyrite 2b (Figure 3F,G) that is coeval with native gold, chalcopyrite, and aikinite formation in large fractures. Later quartz-carbonate veins cut all previous stages. They are composed of quartz, Fe-dolomite, and/or calcite, and they are associated to late reverse movement. Picanço [16] also identified the presence of bornite, galena, covellite, chalcocite, digenite, arsenopyrite, Fe-oxides, and clay minerals such as illite, vermiculite, and smectite; however, these minerals were not observed in this study.
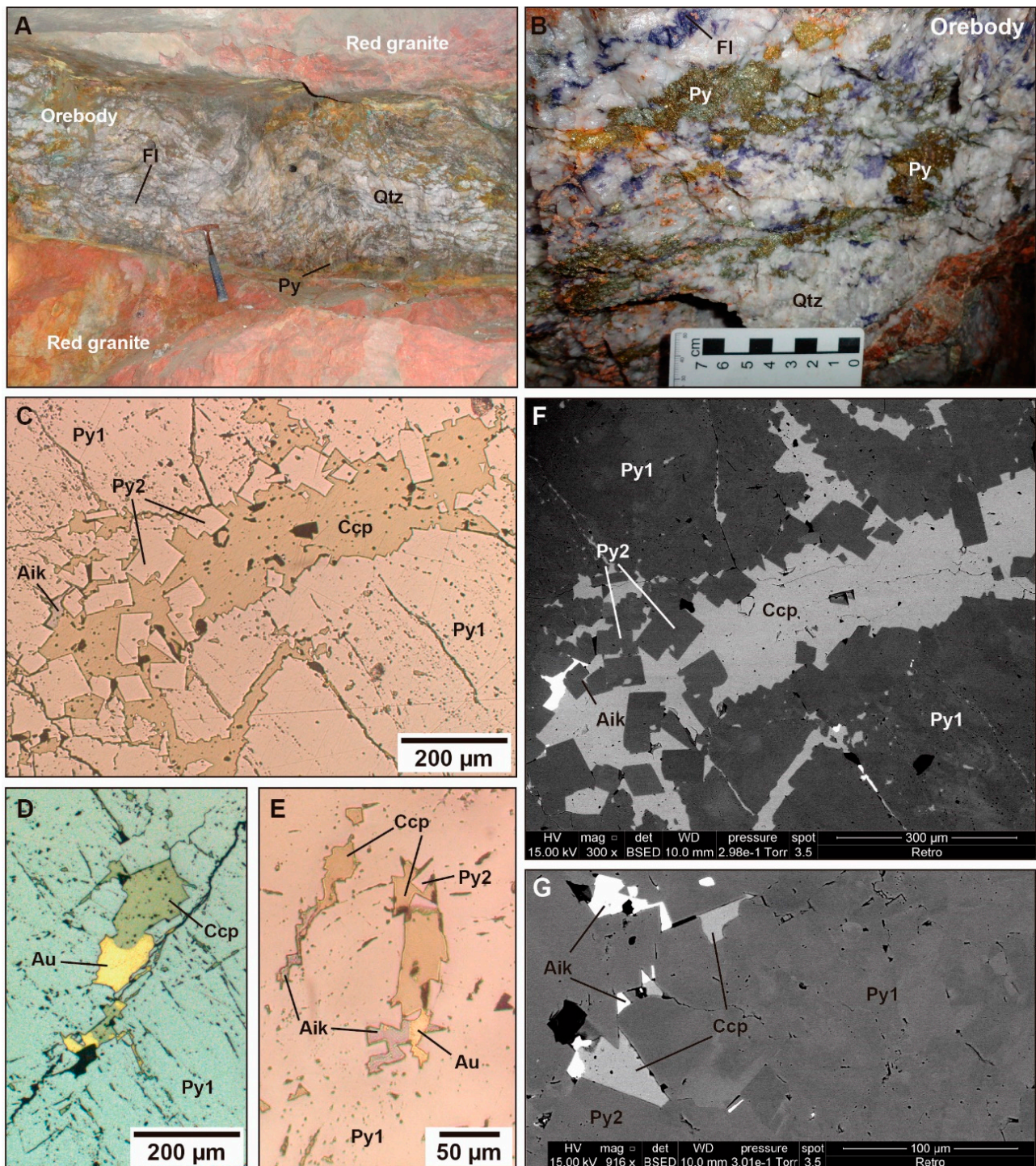
Figure 3. (**A**) Ore vein composed mainly of quartz, sulphides (pyrite, chalcopyrite), and fluorite (outcrop view); (**B**) Photograph of a quartz vein with the ore paragenesis at the outcrop; (**C**) Photomicrograph of the ore paragenesis showing the two pyrite generations (Py2a, Py2b), chalcopyrite, aikinite, and gold; (**D,E**) Photomicrographs of the ore paragenesis of pyrite + gold + chalcopyrite (**D**) and pyrite + gold + chalcopyrite + aikinite (**E**); Figures (**F,G**) are SEM/BSE images showing the distribution of pyrite 2a, pyrite 2b, chalcopyrite, and aikinite. Images (**C–E**): optical microscopy—reflected light, natural light. Abbreviations: Aik—aikinite; Au—gold; Ccp—chalcopyrite; Fl—fluorite; Py2a—pyrite 2a; Py2b—pyrite 2b; Qtz—quartz.

4.1.3. Chemistry of Ore Minerals (EPMA and LA-ICP-MS Analyses)

EPMA analyses show that native gold grains are composed of Au (78.93–85.81 wt %) and Ag (12.99–19.60 wt %) (Figure 4), showing a negative linear trend, also observed by [49]. Aikinite, a Cu-Pb-Bi sulfosalt, has been also detected in thin section, and it is systematically closely associated with visible gold grains (Figure 3D,E; [17]). The association Au-Cu-Bi-Pb was also observed by [15,16] in the Passa Três deposit and in the San Juan de Chorunga gold deposit [49], and such a spatial association between Au and Bi-rich minerals is a common characteristic of mesothermal and IRGD gold deposits [6]. The minor amounts of Cu, Fe and S were observed in native gold.
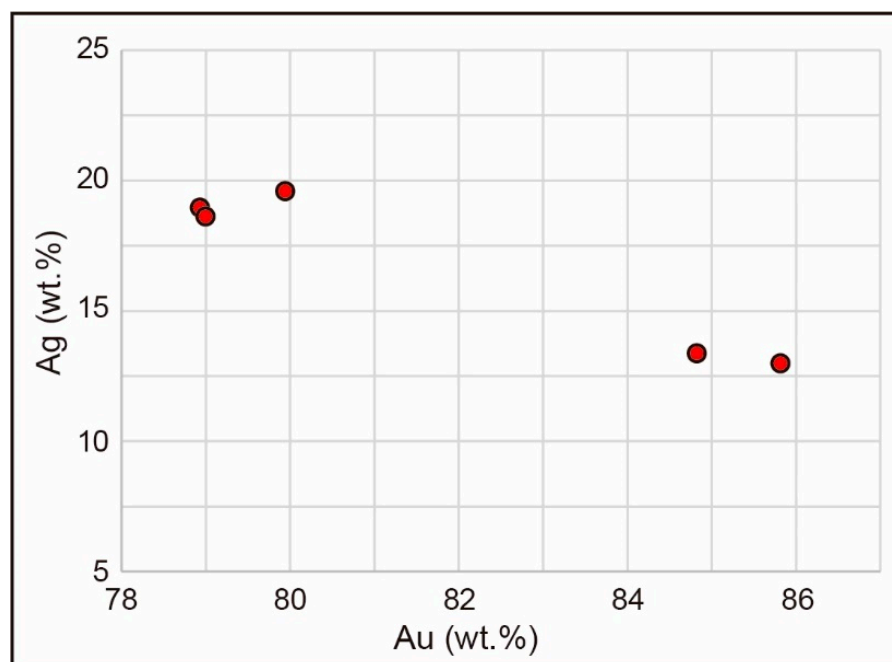

Figure 4. Electron probe microanalyses (EPMA) of gold grains in association with pyrite 2a, pyrite 2b, chalcopyrite, and aikinite. The full EPMA dataset is presented in Supplementary Material B (Table S1).

Due to the suspicion of invisible gold in pyrite 2a (visible gold was only associated with Pyrite 2b), LA-ICP-MS analyses were performed on most sulphide minerals from the gold-bearing assemblage in order to identify potential gold carriers (Supplementary Material C: Table S2). These analyses confirm the presence of invisible gold in pyrites 2a and 2b (Figure 5A,B). The low As and the low Au contents in the two generations of pyrite indicate the presence of chemisorbed invisible gold fixed in structural defects of the pyrite structure (Figure 5B; [50]). Both pyrite generations show similar trace element signatures, including As and Au, and thus geochemically cannot be well differentiated (Figure 5A,B). In the studied pyrite generations, Au correlates positively with Ag (Figure 5C), but in a ratio of 1:10, thus excluding the possibility of incorporating gold as sub-micron inclusions with similar composition as the visible gold in the assemblage.
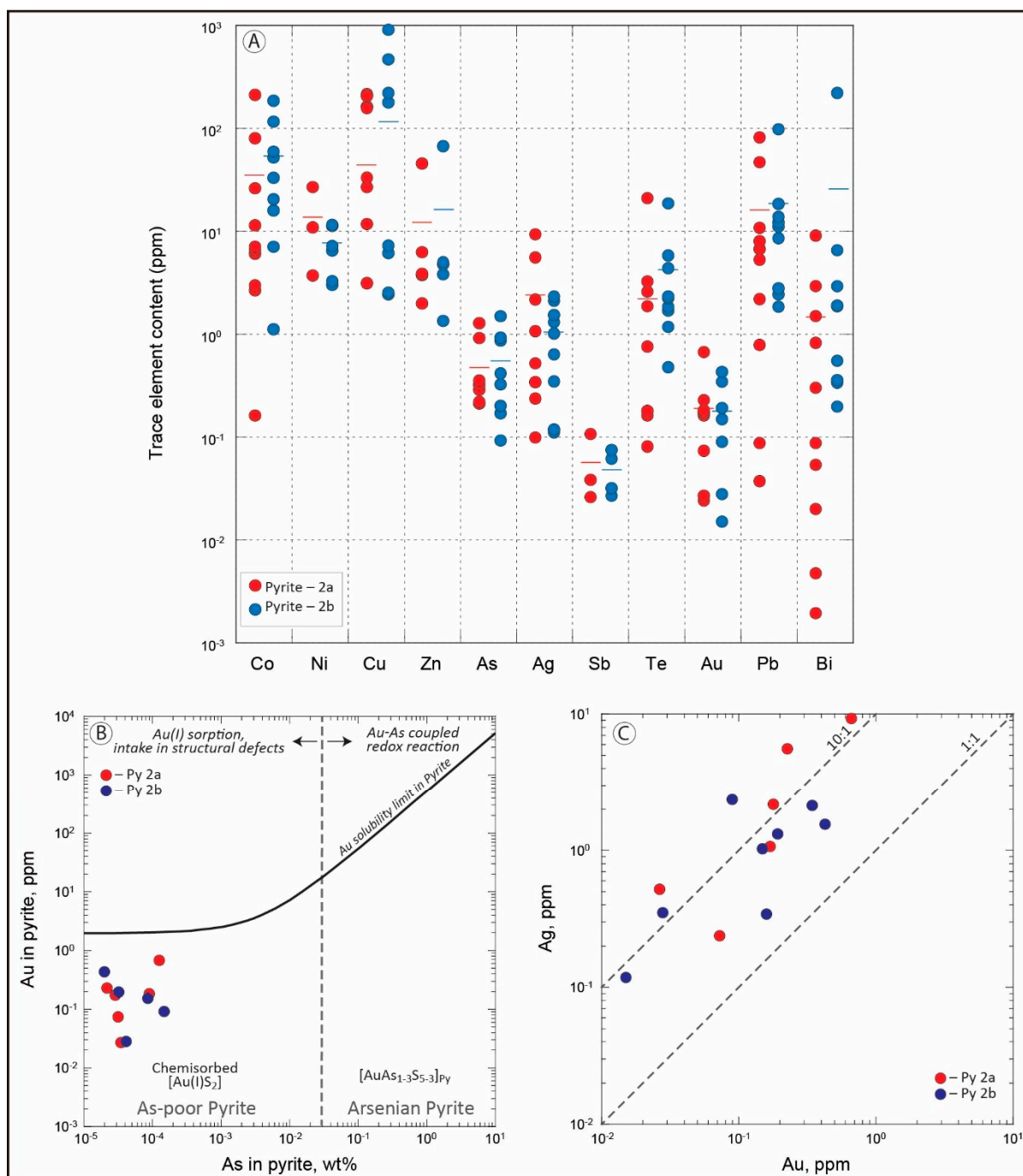
Figure 5. Trace element distribution in pyrite generations 2a and 2b (full dataset available in Supplementary Material C: Table S2): (**A**) Trace element content by pyrite generation (in ppm). Horizontal bars correspond to average values; (**B**) As vs. Au content in pyrite (modified from [50]; gold solubility limit in pyrite from [51]); (**C**) Au vs. Ag content in pyrite.

4.2. Alteration Styles

In the Barreiro zone, two types of alteration that affected the red colour granite of the Passa Três intrusion have been recognised. Their distribution along a vertical section is represented in Figure 6, which is based mainly on drill core observations. The upper part of each section systematically shows abundant markers of late-magmatic and magmatic–hydrothermal features such as UST, pegmatite pockets, and intense quartz-rich veining assimilated to stockscheider. These textures have been interpreted as typical for a granite cupola environment [10]. The two stages of hydrothermal alteration, associated with the

mineralisation, were identified as phengite–quartz–carbonate (PQC) and sericite–carbonate–chlorite (SCC) alterations (Figure 6), based on petrographic observations, QEMSCAN, EPMA, lithogeochemistry, and SEM analyses. The PQC alteration is only developed within narrow grey colour zones frequently parallel to the earlier barren quartz veins during magmatic–hydrothermal transition. Conversely, the SCC alteration is characterised by a greenish colour zone, occurring systematically close to the mineralised veins and frequently associated to breccias.
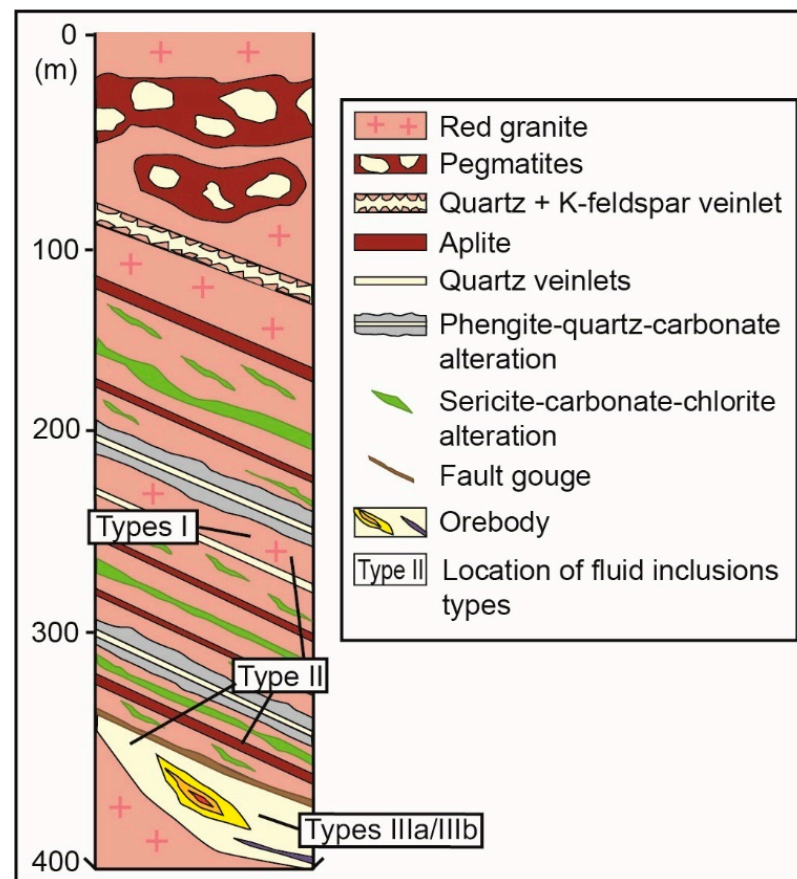

Figure 6. Schematic and synthetic sketch of drill hole vertical section showing the distribution of the main alteration zones and mineralised veins in the Barreiro zone.

In the next two sections, phengite–quartz–carbonate and sericite–carbonate–chlorite alterations will be described. The red granite igneous paragenesis and the hydrothermal alteration assemblages are reported in Figure 7. Quantitative QEMSCAN mineralogical maps of the red granite affected by both alterations' styles are presented in Supplementary Material A (Figures S2 and S3).
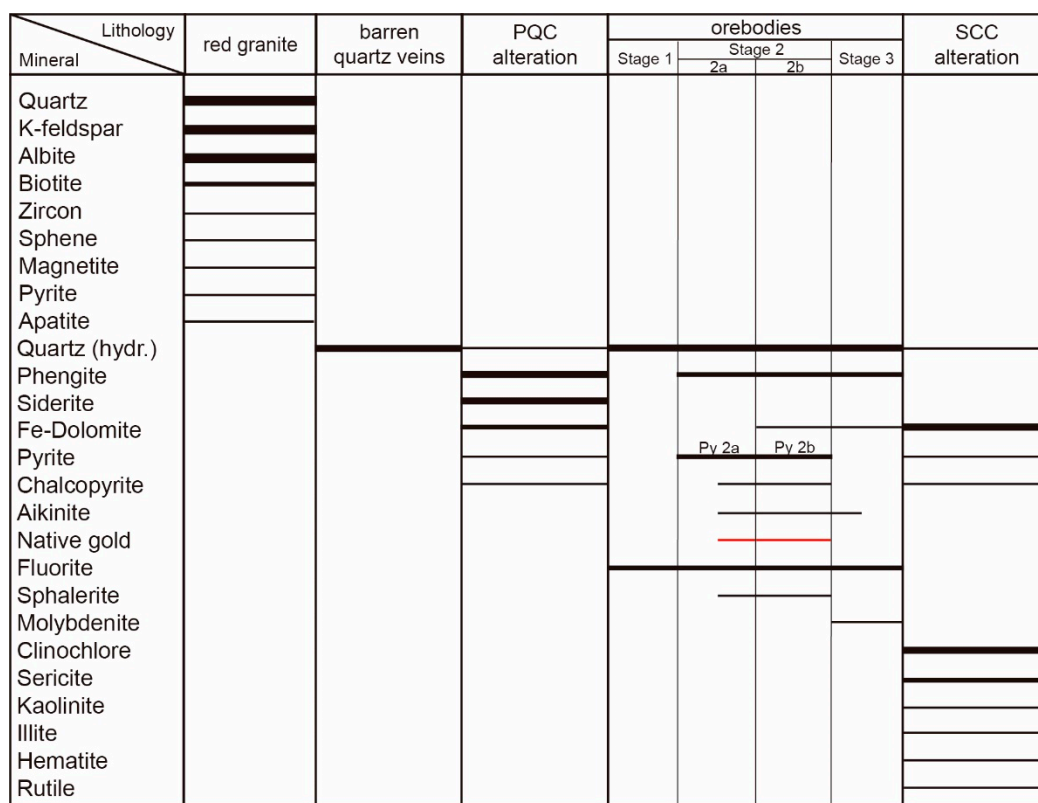
Mineral \ Lithology	red granite	barren quartz veins	PQC alteration	orebodies				SCC alteration
				Stage 1	Stage 2 2a	Stage 2 2b	Stage 3	
Quartz	▬							
K-feldspar	▬							
Albite	▬							
Biotite	—							
Zircon	—							
Sphene	—							
Magnetite	—							
Pyrite	—							
Apatite	—							
Quartz (hydr.)		▬						
Phengite			▬		—			▬
Siderite			▬					
Fe-Dolomite			—					
Pyrite			—		Py 2a	Py 2b		
Chalcopyrite			—		—			
Aikinite					—			
Native gold					—			
Fluorite				—				
Sphalerite					—			
Molybdenite							—	
Clinochlore								▬
Sericite								—
Kaolinite								—
Illite								—
Hematite								—
Rutile								—

Figure 7. Paragenetic sequence of the red granite, barren quartz veins, mineralized veins, and hydrothermal alteration at the Passa Três gold deposit. The width of the solid lines denotes the relative abundance of minerals. The late argillic alteration in the deposit is not indicated. Criteria for differentiation between phengite and sericite is based on grain size.

4.2.1. Phengite–Quartz–Carbonate (PQC) Alteration

This alteration style has been identified in the Passa Três granite as grey alteration halos of 10 cm and alteration bands parallel to barren quartz veins (Figure 8A) of the magmatic–hydrothermal stage (1 to 5 cm width) or as a diffuse alteration within the red granite (Figure 8B). The quartz veins post-date the late-magmatic aplites and pegmatites but pre-date the mineralisation. In the studied drill cores, their abundancy increases at the vicinity of mineralised veins. Barren quartz veins are less abundant in the deeper part of the drill holes, but the grey alteration is still present. As a result of the very localised development of the grey halos, the intensity of this alteration looks moderate.

Mineralogically, these alteration zones are composed of phengite + siderite (Fe(Mg) carbonate) + Fe-dolomite (Ca-Mg-Fe carbonate) + chalcopyrite + quartz ± pyrite (Figure 7). Altered rocks are characterised by relict K-feldspar (partially transformed) and total transformation of plagioclase to phengite (Figure 8C,D). The original igneous texture was largely obliterated, with phengite replacing plagioclase, microcline, and biotite. Biotite is replaced by phengite, siderite, Fe-dolomite, quartz, and rutile (Supplementary Material A, Figure S4). Primary K-feldspar crystals are anhedral, and quartz grains may present brittle deformation, such as fractures. Secondary non-deformed quartz is common. Only rare sulphide minerals are associated with this alteration, with some sparse pyrite and chalcopyrite crystals. As a result of the strong alteration and disappearance of K-feldspar, plagioclase, and biotite associated with the formation of abundant phengite, siderite, and Fe-dolomite, this alteration style has been defined as phengite–quartz–carbonate alteration.
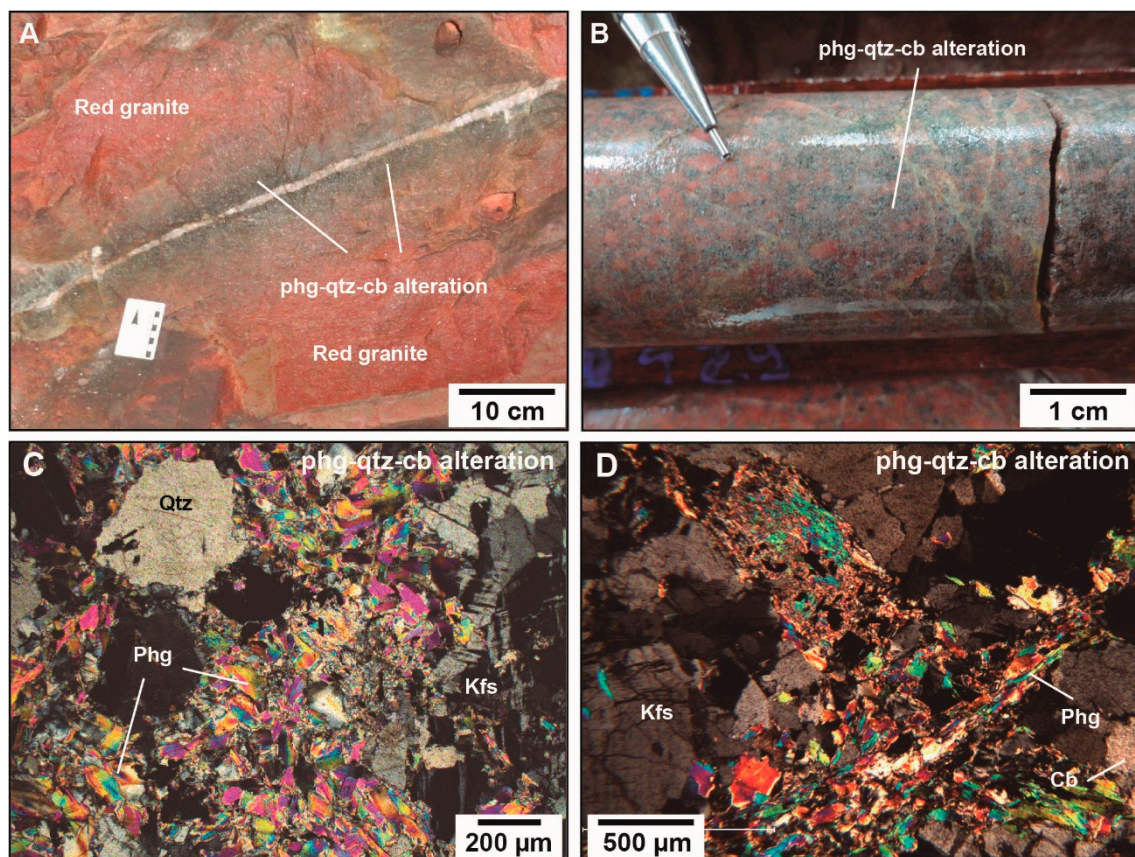
Figure 8. Phengite–quartz–carbonate (PQC) alteration associated to gold mineralisation in the Passa Três granite: (**A**) PQC alteration halo along a barren quartz vein (underground mine level 3); (**B**) PQC alteration in borehole resulting in a grey colour of the Passa Três granite; (**C**) Photomicrograph showing the development of small phengite crystals as an alteration of K-feldspar and plagioclase in a medium-grained isotropic texture; (**D**) Two fractures underlined by the concentration of phengite crystals as part of the PQC alteration. Images (**C**,**D**): optical microscope—polarised light. Abbreviations: Cb—carbonate; Kfs—K-feldspar; Phg—phengite; Qtz—quartz.

4.2.2. Sericite–Carbonate–Chlorite (SCC) Alteration

The sericite–carbonate–chlorite alteration is characterised by the complex assemblage of sericite + clinochlore + Fe-dolomite (Ca-Mg-Fe carbonate) + quartz + hematite + rutile + kaolinite ± pyrite ± chalcopyrite ± illite. The medium scale (up to 10 metres) diffusive SCC halos developed parallel to the main mineralised fault structures have a greenish colour (Figure 9). In drill cores, the SCC alteration presents a zebra pattern following planes parallel to the mineralised veins (Figure 9A,C,D). The intensity of this alteration varies greatly but increases close to the orebodies, which are associated to the presence of breccias along the contact of the mineralised veins (Figures 9B and 10A–D). The alteration is texturally destructive; thus, the original igneous texture of the host granite is no longer observable. Brittle deformation results in the fracturing of K-feldspar and plagioclase and undulose extinction in quartz crystals. Most quartz and K-feldspar grains are broken, exhibiting irregular shapes and highly variable grain sizes, also indicating brittle deformation. Recrystallised quartz sub-grains have been also identified.
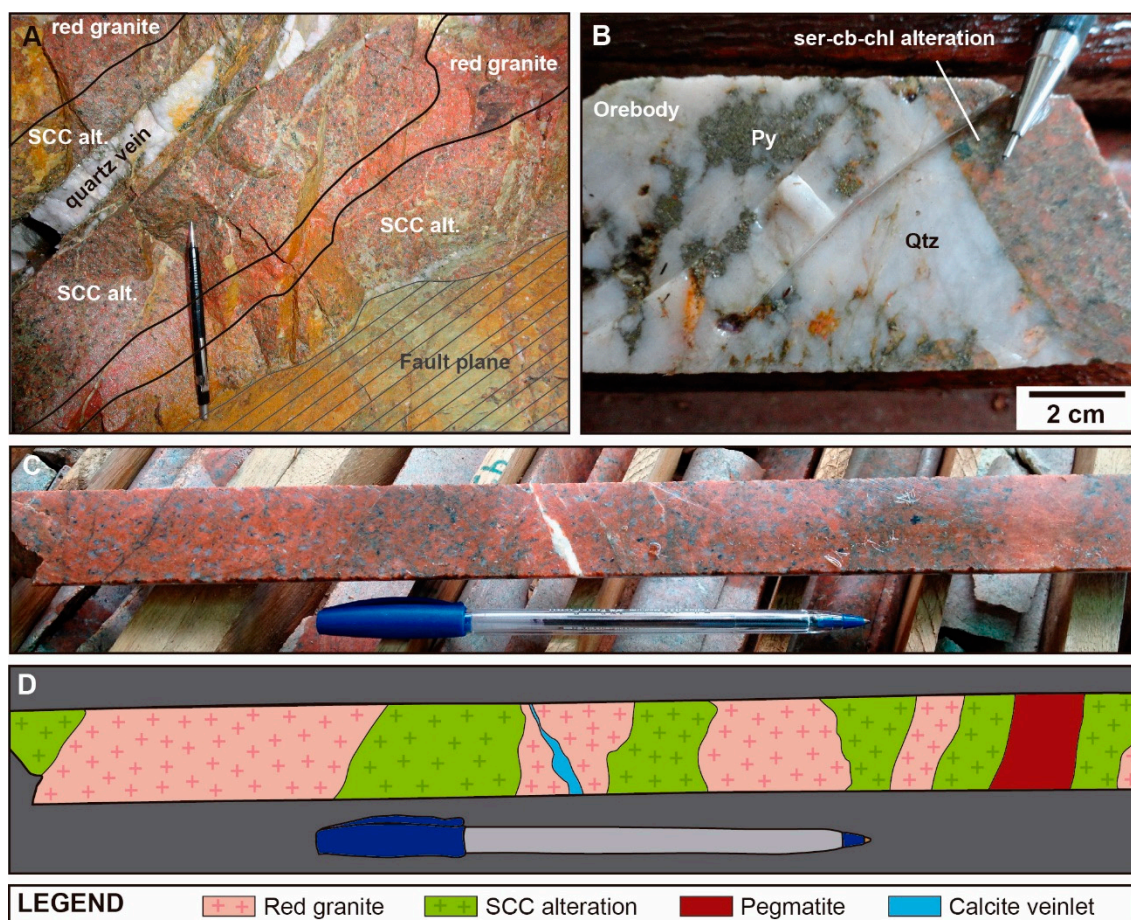
Figure 9. Sericite–carbonate–chlorite (SCC) alteration in the Passa Três deposit: (**A**) Zebra pattern formed by the alternation of greenish granite (SCC alteration) and red granite near orebody; (**B**) SCC alteration along the border of a quartz–sulphide vein (borehole sample); (**C,D**) Drill core sample exhibiting zebra-pattern (**C**) and its schematic drawing (**D**). Abbreviations: Py—pyrite; Qtz—quartz.

In thin section, phengite and carbonate are observed in small fractures that cut the original igneous texture and the earlier phengite–quartz–carbonate alteration (Figure 10E,F). In addition, biotite was partly or totally replaced by Fe-dolomite, chlorite, and apatite (Supplementary Material A, Figure S5) (see Section 6), and plagioclase was transformed to sericite along hairline cracks (similar to K-feldspar). Regardless of the alteration intensity, sericite and other minerals such as Fe-dolomite can also form thin veinlets. A small amount of chalcopyrite occurs as disseminations. Strong SCC alteration develops along the border of mineralised veins as well as along cracks and/or open space in the breccia matrix (Figure 10A–D) but also in granite clasts inside the main veins. The main sulphides associated with this alteration style are pyrite and chalcopyrite that occur as subhedral/euhedral grains. Due to its spatial association with mineralisation, this alteration is believed to be contemporaneous to the formation of the gold mineralisation within pull-apart structures formed by normal faulting [10].
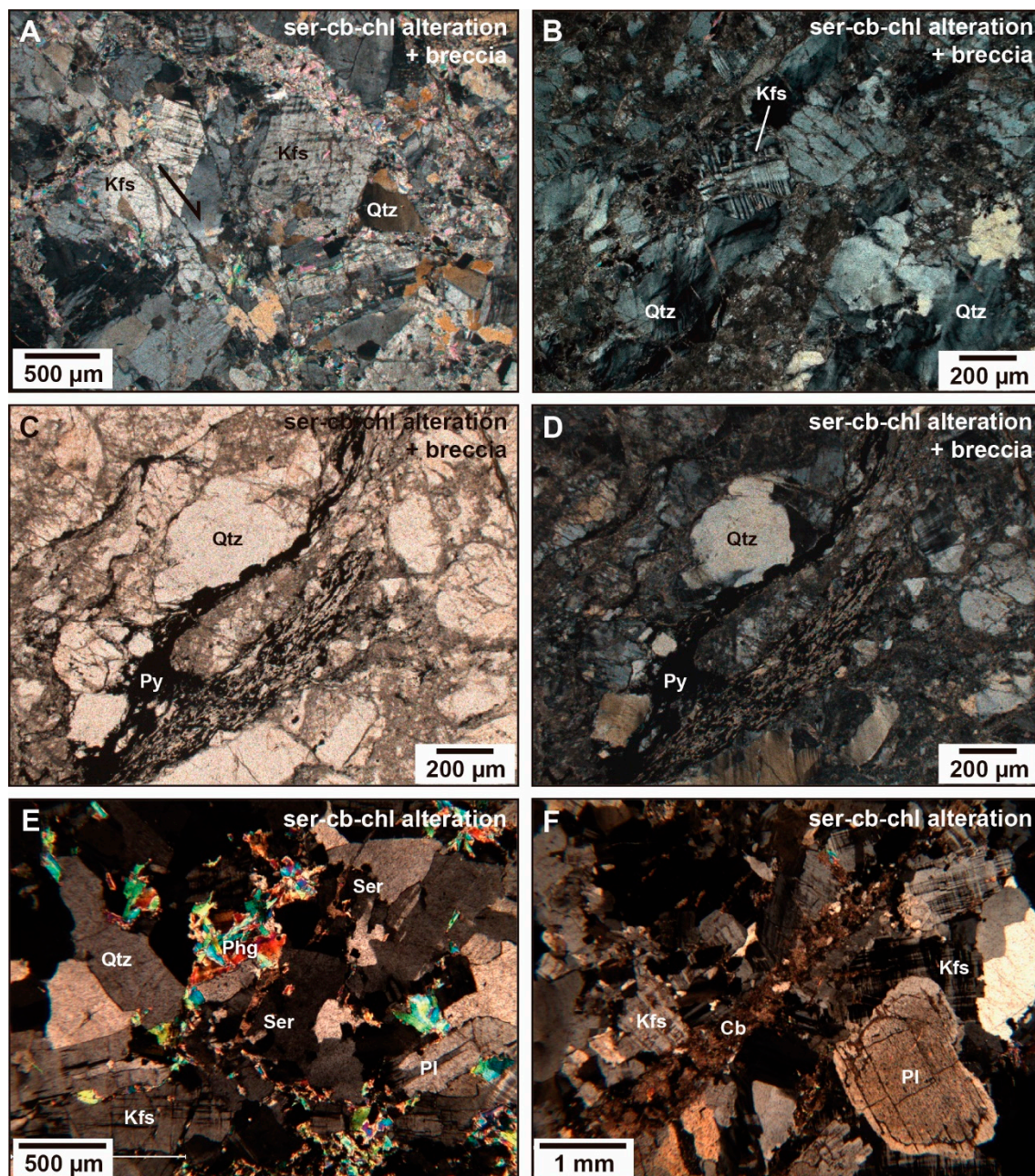
Figure 10. Microscopic aspects of the SCC alteration in the Passa Três deposit: (**A**) to (**D**) SCC alteration superimposed and/or forming breccia (red granite) at the border of the orebody with some evidence of normal faulting (**A**), fractured K-feldspar crystal (**B**) and formation of pyrite-rich levels (**C**,**D**); (**E**) SCC alteration with sericite planes affecting the texture of the granite; (**F**) Carbonate planes associated to the SCC alteration. Images (**A**–**F**) optical microscope—natural (**C**) and polarised (**A**,**B**,**D**–**F**) light. Abbreviations: Cb—carbonate; Chl—chlorite; Kfs—K-feldspar; Phg—phengite; Pl—plagioclase; Py—pyrite; Qtz—quartz; Ser—sericite.

4.2.3. Fault Gouge

The brown-coloured fault gouge occurs in the normal fault planes that shelter the orebodies (N-S/60–75 W; E-W/45–70 S) [10] and at the borders of millimetres to 1-centimetre-thick veins (Figure 11A,B). The fault gouge is 0.2 to 3.0 mm thick and is formed due to the movements along the fault zones but also to their re-activation, which also led to brittle deformation and breccia formation along the vein borders, in the host rock (red granite) [10,17]. The fault gouge mainly consists of clay minerals and sulphides, mainly pyrite, and these

minerals are interpreted as post-dating the mineralisation, as it crosscuts the other alterations. The fault gouge is used as a guide by the mine geologists to find the orebodies.
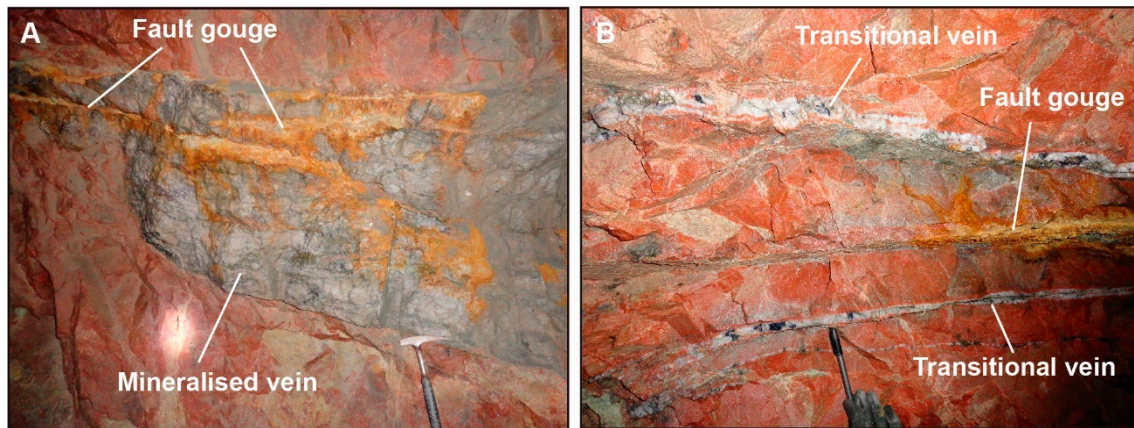

Figure 11. (**A**) Orebody with late fault gouge with an ochre colour; (**B**) Fault gouge associated with fault plane near transitional veins (see definition in [10]).

4.3. Mineral Chemistry

EPMA analyses have been performed on igneous minerals (K-feldspar, plagioclase, and biotite) and alteration minerals (chlorite, white mica, and carbonate). The location of analytical points is reported in Figure 12, and the results are presented in the Supplementary Material D (Tables S3–S7 and Figures S6–S9).
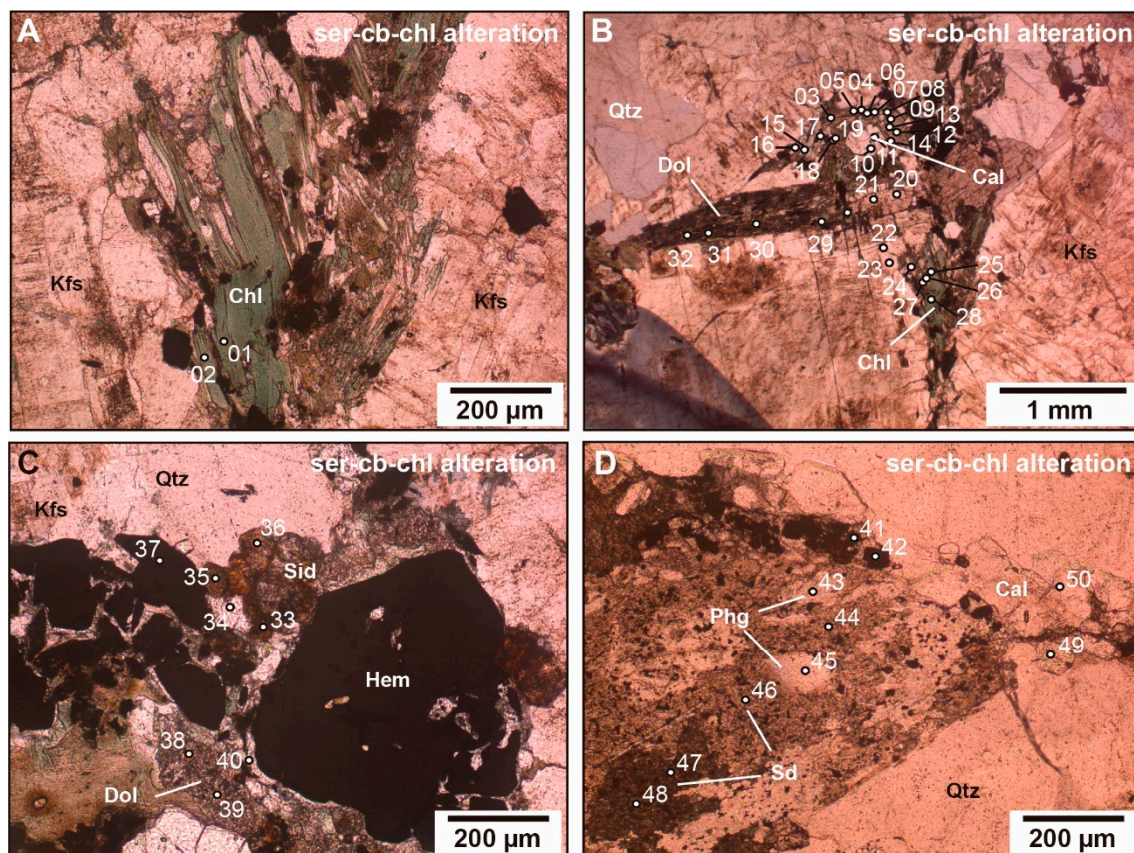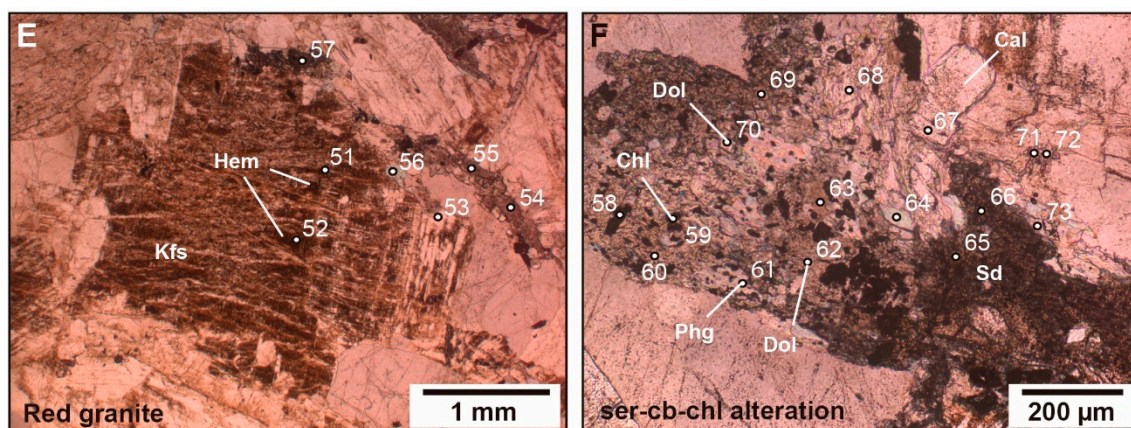

Figure 12. *Cont*.

Figure 12. Thin section photomicrographs of SCC alteration minerals of the Passa Três granite analysed by EPMA: (**A**) Chlorite replacing magmatic biotite; (**B**) Mafic aggregate in red granite formed by biotite and altered amphibole; analytical points indicate the presence of clinochlore, siderite (Fe(Mg) carbonate), Fe-dolomite (Ca-Mg-Fe carbonate), and calcite as alteration minerals; (**C**) Fe-dolomite (Ca-Mg-Fe carbonate) and siderite (Fe(Mg) carbonate) as alteration in the red granite; (**D**) Relic sphene crystal altered to siderite (Fe(Mg) carbonate), phengite, Fe-dolomite (Ca-Mg-Fe carbonate), and rutile, SCC alteration; (**E**) K-feldspar with Fe-oxide exsolution as indicated by the presence of FeO in the EPMA analysis; (**F**) Biotite replaced by clinochlore, calcite, Fe-dolomite, siderite, sericite (phengite), with indication of the points of analyses. Images (**A**–**F**): optical microscope—natural light. Abbreviations: Cal—calcite; Cb—carbonate; Chl—chlorite; Dol—Fe-dolomite; Hem—hematite; Kfs—K-feldspar; Phg—phengite; Qtz—quartz; Sd—siderite; Ser—sericite.

4.3.1. Chlorite

Chlorite crystals associated to the sericite–carbonate–chlorite alteration assemblage have been analysed (Figure 12A,B,F; Supplementary Material D: Table S3 and Figure S6). Chlorites have mostly a clinochlore composition and display the following average structural formula calculated on the basis of 14 oxygens $(K_{0.02}Na_{0.22}Mg_{2.07}Fe_{1.85}Al^{VI}_{1.17}Ti_{0.13})[(Si_{3.22}Al^{IV}_{0.78})O_{10}]$ $(OH_{1.73},F_{0.27})$. Only one point has been encountered with chamosite composition, but the habitus looks to be similar to the other chlorite types in the deposit.

The chlorite geothermometer of Cathelineau et al. [52] has been applied, suggesting temperatures of formation between 264 and 335 °C for chlorite associated to alteration and gold mineralisation, with an average value of 310 °C.

4.3.2. Biotite

Two magmatic biotite crystals have been analysed from the core of the red granite (Figure 12B; Supplementary material D: Table S4). Results indicate an average structural formula $(K_{1.75}Na_{0.01})(Fe^{II}_{0.06} Mg_{3.32})(Fe^{III}_{1.71}Al^{VI}_{0.00} Ti_{0.28})[Si_{5.48}Al^{IV}_{2.04}O_{20}](OH_{2.18},F_{1.82})$ consistent with classical magmatic biotite.

4.3.3. Carbonate

Based on the QEMSCAN analyses, two main alteration-related carbonate minerals were identified: Ca-Mg-Fe carbonate and Fe(Mg) carbonate, with some calcite (Figure 12C,D). These carbonates were analysed by EPMA, and Ca-Mg-Fe carbonate and Fe(Mg) carbonate were recognised as Fe-dolomite and siderite, respectively (Figure 12C). Both Fe-dolomite and siderite compositions are characteristic of the carbonate associated with the phengite–quartz–carbonate alteration. Fractures associated with the sericite–carbonate–chlorite alteration are filled mostly by Fe-dolomite and calcite with the scarce occurrence of siderite. Carbonate appears as one of the major mineral phases attributed to the alteration processes. Table S5 (Supplementary material D) shows Fe-dolomite, calcite, and siderite analyses and calculated structural formulas related to the sericite–carbonate–

chlorite alteration, which are graphically represented in the ternary Ca-Mg-Fe diagram (Supplementary material D: Figure S7).

4.3.4. Feldspars

K-feldspar has been analysed in the red granite (Figure 12E) and transitional veins (Supplementary Material D: Table S6 and Figure S8). K-feldspar crystals of the red granite yield an average formula $(K_{1.01}Na_{0.03})[Al_{1.00}Si_{2.97}O_8]$. As these crystals present chess board texture, microcline is suspected. K-feldspar grains occurring along the contacts of the transitional veins have a similar composition $(K_{1.03}Na_{0.03})[Al_{1.00}Si_{2.99}O_8]$ and also present a chess board texture. Albite has been also detected within the red granite (formula $(K_{0.01}Na_{0.95})[Al_{1.01}Si_{2.98}O_8]$) and in a sample affected by the sericite–carbonate–chlorite alteration, with a structural formula $(K_{0.01}Na_{0.92})[Al_{1.04}Si_{2.96}O_8]$ (Supplementary Material D: Table S6 and Figure S8), and in both cases, it was considered as a magmatic in origin, not affected by alteration.

4.3.5. White Mica (Phengite)

Table S7 (Supplementary Material D) summarises the analyses of white mica associated to the sericite–carbonate–chlorite alteration and the transitional veins. White mica from the transitional veins has the following average structural formula: $(K_{2.03}Na_{0.03})(Fe_{0.59}Mg_{0.55}Al^{VI}_{2.92}Ti_{0.10})[Si_{6.81}Al^{IV}_{1.19}O_{20}](OH,F)_4$, while the mineral associated with the sericite–carbonate–chlorite alteration has a composition $(K_{1.53}Na_{0.02})(Fe_{0.33}Mg_{0.43}Al^{VI}_{3.10}Ti_{0.04})[Si_{6.70}Al^{IV}_{1.30}O_{20}](OH_{3.58},F_{0.42})$. All analysed white mica aggregates are di-octahedral mica according to the criteria of Deer et al. [53]. Indeed, such a homogeneity among the white mica compositions from the transitional veins and the sericite–chlorite–carbonate alteration zones (Figure 12F) suggests that they are formed by fluids with similar composition. When plotted in a white mica discrimination diagram, all analytical points plot in the phengite field (Supplementary Material D: Figure S9); therefore, it is the composition assumed for the white mica throughout this work.

4.4. Mass Balance of Hydrothermal Alterations

In order to estimate the chemical changes associated with the main alteration types (phengite–quartz–carbonate and sericite–carbonate–chlorite alterations), major (Si, Al, Fe, Mg, Ca, Na, K, and P), light-lithophile elements (LILEs; e.g., Cs, Rb, Sr, Ba, Pb, and U) and transition metals (TRTEs; e.g., Sc, V, Cr, Co, Ni, Cu, and Zn) were analysed both in representative alteration samples and in least-altered rock analogues by XRF. The least altered sample corresponds to the red granite. The method of MacLean [54] was applied to calculate the mass balance between altered rocks and their protolith. Zirconium was chosen as an immobile element for the calculations. Bulk rock analyses and mass balance calculation results are presented in the Supplementary Material E (Table S8).

4.4.1. Phengite–Quartz–Carbonate Alteration

Losses and gains associated with the phengite–quartz–carbonate alteration are presented in Table S8 (Supplementary Material E) and Figure 13A. Gains in K_2O and Rb and loss in Na_2O, CaO, and Sr, as well as a slight increase in LOI (loss on ignition), are related to the replacement of plagioclase by phengite. The breakdown of biotite and its replacement by chlorite in parallel to the crystallisation of Fe-dolomite and siderite (Fe- and Mg-bearing carbonates) results in significant gain of Fe_2O_3, MgO, and MnO. TiO_2 content remains constant, reflecting its immobile behaviour; despite the consumption of sphene, rutile crystallised. The slight enrichment in P_2O_5 is probably due to the crystallisation of apatite. SiO_2 gain is probably related to the crystallisation of quartz observed near the consumed biotite crystals.
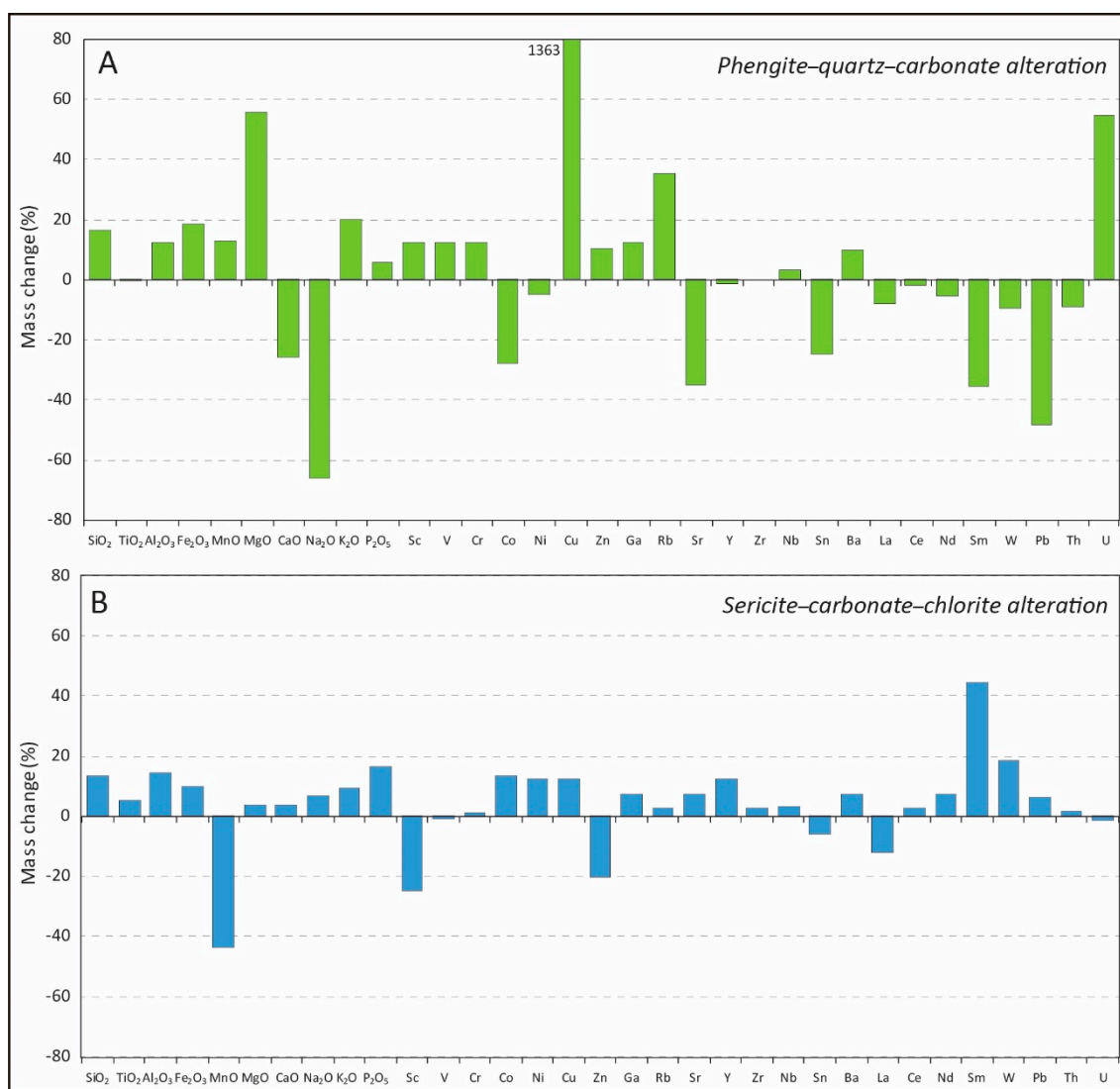
Figure 13. Mass balance diagrams—gain and loss for (**A**) phengite–quartz–carbonate and (**B**) sericite–carbonate–chlorite alterations.

Copper shows an important gain due to the precipitation of disseminated chalcopyrite. Lanthanum and Sm loss could be associated to the breakdown of sphene. Some transitional elements, such as Zn, Cr, V, and Sc, present slight gains, which is possibly due to the precipitation of hydrothermal sulphides. The losses in Ni, Sn, and Co may be attributed to the destabilisation of magmatic oxides such as magnetite and ilmenite.

4.4.2. Sericite–Carbonate–Chlorite Alteration

Mass balance calculations for the sericite–carbonate–chlorite alteration are presented in Table S8 (Supplementary Material E) and Figure 13B. A gain in SiO_2 and Al_2O_3 is related to the precipitation of quartz and Al minerals (sericite, chlorite), respectively. A small TiO_2 gain is related to the crystallisation of rutile following the consumption of sphene and magnetite. A slight increase in Fe_2O_3 and MgO contents is due to the precipitation of chlorite after biotite as well as siderite and Fe-dolomite. Manganese loss probably relates to the alteration of biotite and magnetite, although the Fe_2O_3 content remains constant because of siderite formation. A gain of Cu shows that chalcopyrite can crystallise, as confirmed by optical microscopy. The formation of other sulphides is suspected by a slight gain of Co and Ni. A gain in P_2O_5 agrees with the crystallisation of apatite, which is possibly also associated with Sm gain. In addition, the increase in LOI is associated with

the crystallisation of carbonate (Fe-dolomite). Uranium loss is probably also associated to the consumption of sphene. A slight leaching of some transitional elements (e.g., Zn, V, Sc) and Sn may be related to the consumption of other magmatic sulphides.

4.5. Sulphur Isotopes

Sulphur isotope data (δ^{34}S, ‰) were collected on five samples of pyrite and one sample of barite from the gold mineralisation at Passa Três granite. Results are reported in the Supplementary Material G (Figure S10). Pyrite crystals display δ^{34}S values in the restricted range between -0.1‰ and 1.1‰, which is consistent with a magmatic origin for sulphur, and possibly with mantle contribution, indicating a very deep source. Additionally, the barite sample displays a δ^{34}S value of 15.6‰, which is also typical for sulphates precipitating from magmatic fluids. These results are coherent with δ^{34}S analyses from earlier work (Figure 14; [16]) and other geochemical data for the Passa Três granite, which is interpreted as indicating mantle origin for the magma [15].
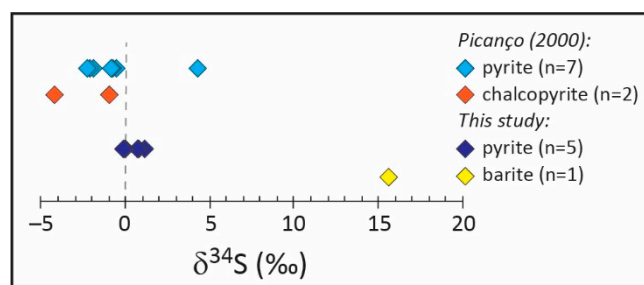

Figure 14. δ^{34}S isotopic composition of pyrite, chalcopyrite, and barite from the Passa Três deposit, data from this study and Picanço [16].

4.6. Fluid Inclusions

Fluid inclusions were studied in mineralised quartz veins cropping out at levels 4 and 5 in the underground mine and also from the surrounded granite and associated aplitic dikes. Quartz is the main mineral of the gangue in which gold is associated with pyrite. Many of the collected samples do not contain abundant fluid inclusions of size suitable for microthermometric measurements (difficulty also reported by Piekarz [15] and attributed to the late brittle deformation of the orebodies), but a few samples were selected for further investigation. Unfortunately, fluid inclusions from the early hydrothermal veins (veins with K-feldspar borders) were too small in size and thus not analysed. Using the petrographic criteria of Roedder [55], the fluid inclusions analysed have been classified as primary and secondary. Fluid inclusion assemblages (FIA) have been defined according to the criteria of Goldstein and Reynolds [56] prior to microthermometry analysis. In an FIA, fluid inclusions are cogenetic and trapped at the same time and are representative of the same fluid. Microthermometric data are summarised in Table 1 and presented in Figures 15–19.
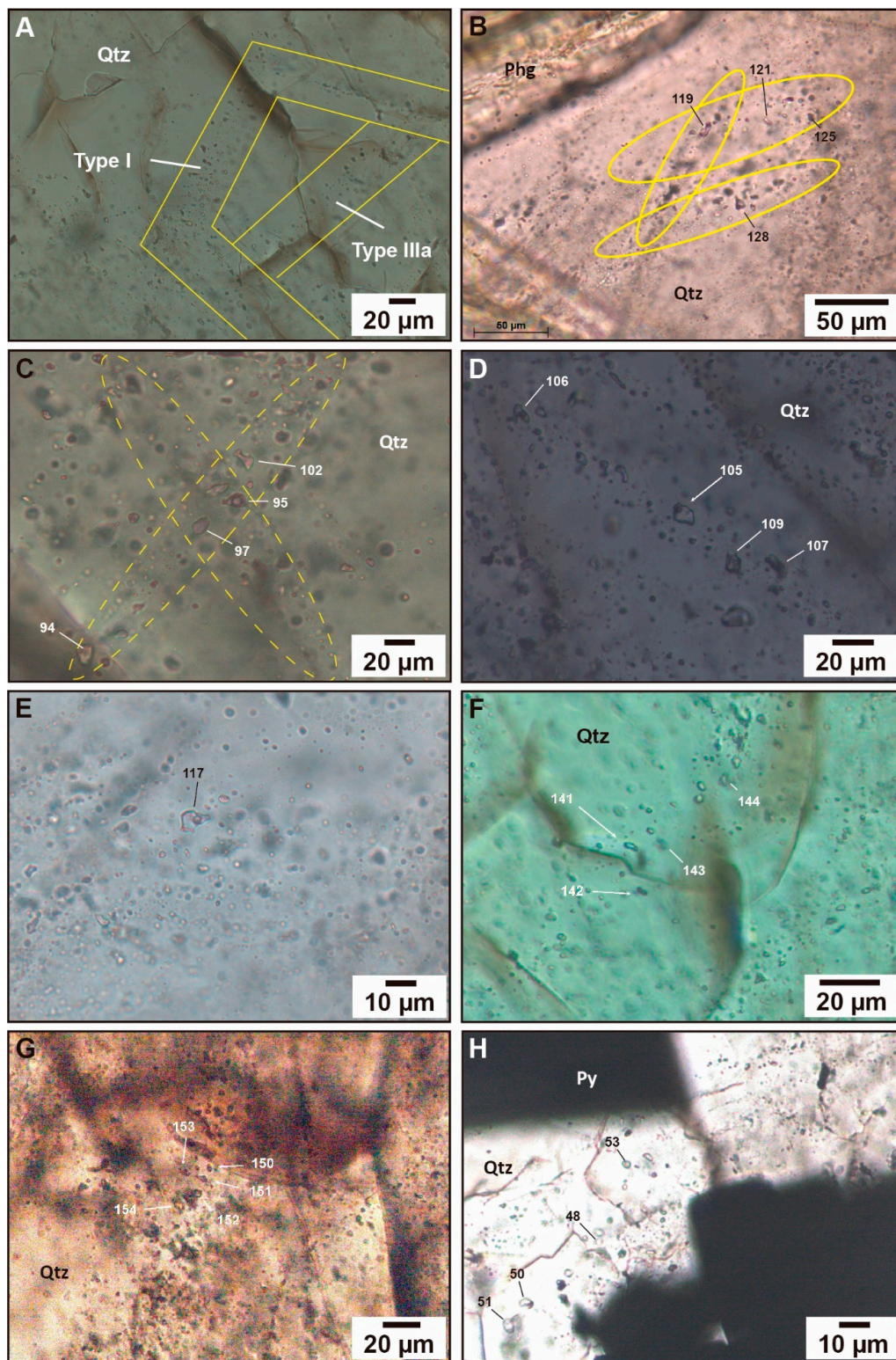
Figure 15. Fluid inclusion petrography of gold mineralisation at the Passa Três gold deposit (Barreiro zone): (**A**) Primary H_2O-CO_2-NaCl (type I) in growth zones in magmatic quartz and secondary type IIIa inclusions as a trail, red granite sample; (**B**) Type II (H_2O-CO_2-NaCl) fluid inclusions in quartz 1 from a mineralised vein; (**C**) Type II (H_2O-CO_2-NaCl) fluid inclusions showing different shapes and vapor/liquid ratio in a granite sample; (**D**) Type II (H_2O-CO_2-NaCl) fluid inclusions showing different

shapes and vapor/liquid ratios in an aplite sample; (**E**) Detail of type II (H_2O-CO_2-NaCl) fluid inclusions (liquid H_2O + vapor CO_2); (**F**) Detailed view of type IIIa (H_2O-NaCl) fluid inclusions (liquid H_2O); (**G**) Type IIIa (H_2O-NaCl) fluid inclusions as clusters in quartz 1 in a mineralised vein; (**H**) Type IIIb (H_2O-NaCl) fluid inclusions in quartz 3 near pyrite crystals within a quartz mineralised vein. Numbers correspond to the analysed fluid inclusions. Images (**A**–**H**): optical microscope—natural light. Abbreviations: Phg—phengite; Qtz—quartz; Py—pyrite.
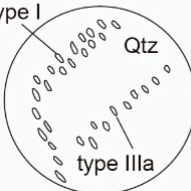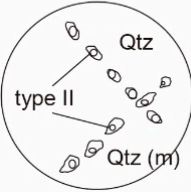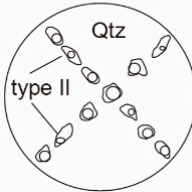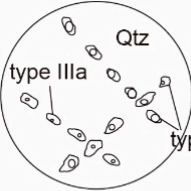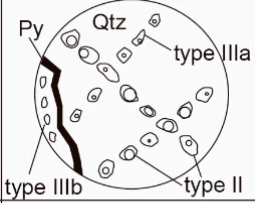
STAGE		MIN.	FLUID INCLUSION TYPE	LITOLOGY RECORDED		
				GRANITE	APLITE	MINERALISED VEIN
MAGMATIC STAGE	Granite	Qtz (m)	Type I (H_2O-CO_2-NaCl) *Primary inclusions*	*[sketch: type I, Qtz, type IIIa]*	X	X
MAGMATIC-HYDROTHERMAL TRANSITION STAGE	UST Aplite Pegmatite Stockscheider Vein (FK border) Barren quartz veins		*not reported*	X	X	X
HYDROTHERMAL MINERALISATION STAGES	Stage 1	Qtz1 (h)	Type II (H_2O-CO_2-NaCl)	*[sketch: type II, Qtz, Qtz (m)]*	*[sketch: type II, Qtz]*	*[sketch: type II, Qtz]*
	Stage 2	Qtz 2 (h)	Type III (H_2O-NaCl)	*[sketch: type IIIa, Qtz, type II]*	X	*[sketch: Py, Qtz, type IIIa, type IIIb, type II]*
	Stage 3	Qtz 3 (h)	*not reported*	X	X	X

Figure 16. Synthetic sketch and paragenetic table showing the relationships and the distribution of the different types of fluid inclusions in the studied samples of the Barreiro zone relative to magmatic–hydrothermal transition. Primary fluid inclusions (type I) are found in magmatic quartz in the host granite; type II fluid inclusions occurs in granite, aplite, as well as in the mineralised quartz vein; types IIIa and IIIb are observed in the granite and mineralised quartz veins. Abbreviations: H—hydrothermal; M—magmatic; Min—mineral; Qtz—quartz; Py—pyrite.
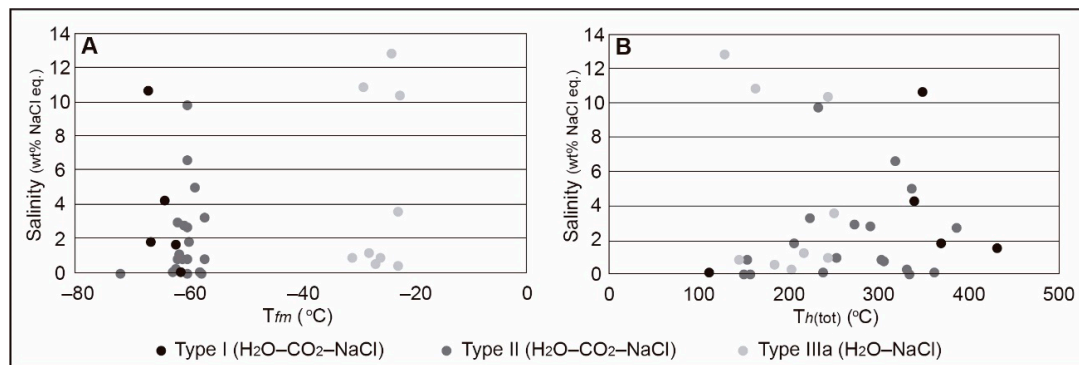
Figure 17. (**A**) Temperature of first melting (T*fm*) vs. salinity diagram for the fluid inclusions of the Passa Três gold deposit; (**B**) Total homogenisation temperature (T*h*-tot) vs. salinity plot of the studied fluid inclusions.
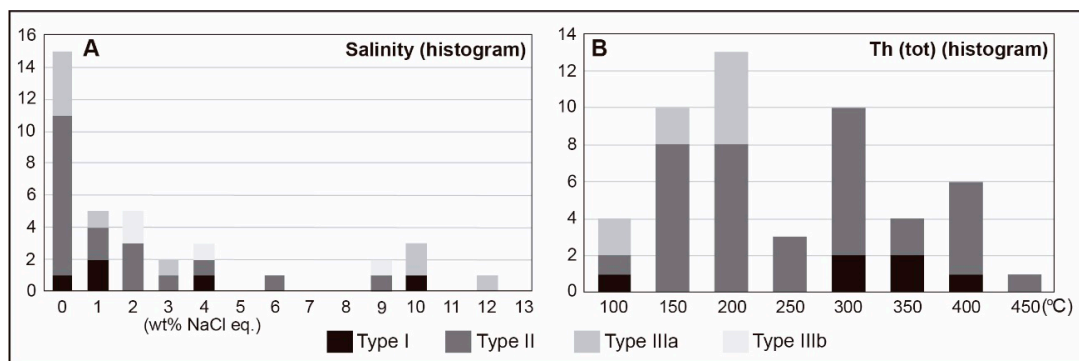

Figure 18. Frequency diagram of (**A**) salinities and (**B**) T*h*-tot of the fluid inclusion types studied in the Passa Três deposit.

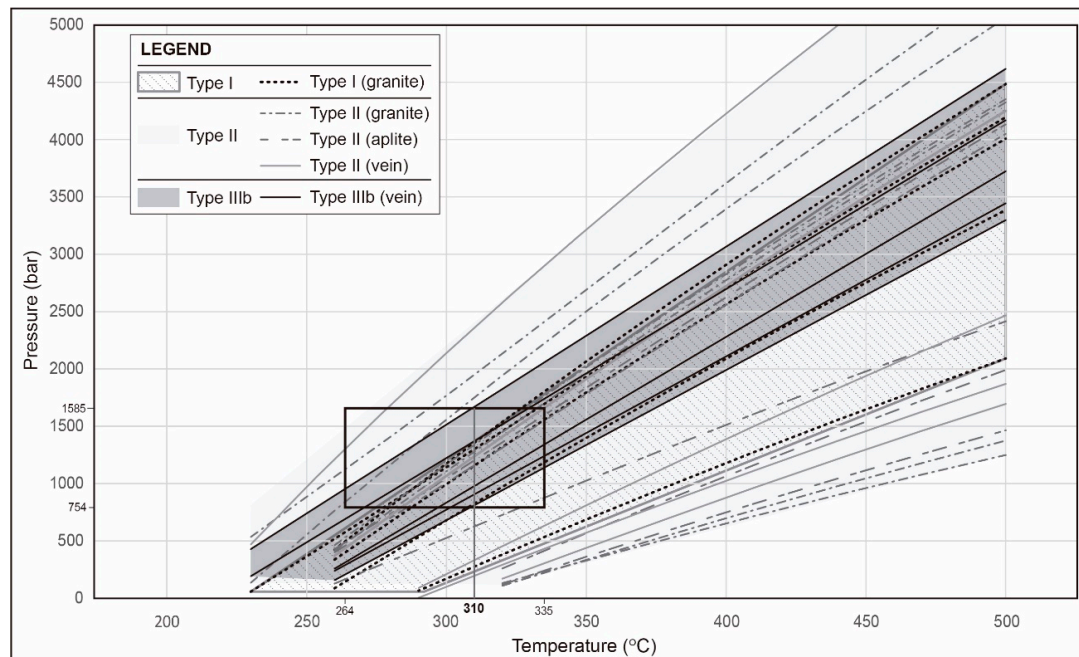**Figure 19.** Pressure–temperature (P-T) diagram with isochores of the different fluid inclusion types in the Passa Três gold deposit. The black rectangle represents entrapment conditions of mainly type IIIb fluid inclusions, those associated with the mineralisation stage, and constraints from chlorite geothermometry (temperatures of formation from 264 to 335 °C; average temperature of 310 °C).

Table 1. Microthermometric results of fluid inclusions in quartz from the Passa Três gold deposit. Abbreviations: Qtz—quartz; T*fm*—first melting temperature; T*m*-clath—CO_2 clathrate melting temperature; T*m*-ice—ice melting temperature; T*h*-tot—total homogenisation temperature.

Sample	Mineral	Lithology	Type	Number	T*fm* (°C)	T*m* clath (°C) (Average)	T*m*-ice (°C) (Average)	T*h*-tot (°C) (Average)	Salinity (wt.% NaCl eq.) (Average)	Density (g/cm³) (Average)
GEF	Quartz	Red granite	I	6	−67.2 to −61.4	4.0 to 16.4 (9.3)	−8.1 to −1.2 (−3.6)	432 to 112 (329.7)	0.04 to 10.63 (3.65)	0.74 to 0.94 (0.87)
GEF	Quartz	Red granite	II	10	−67.6 to −56.0	4.5 to 14.7 (9.3)	−10.2 to −0.2 (−5)	150 to 453 (246.19)	0.40 to 9.77 (2.72)	0.62 to 1.02 (0.88)
BD-76d	Quartz	Aplite	II	14	−64.3 to −57.3	6.3 to 12.2 (9.4)	−11.6 to −1.6 (−6.3)	177 to 430 (301.1)	2.23 to 4.97 (2.64)	0.65 to 1.07 (0.93)
BD-26b	Quartz	Mineralised vein (Qtz 1)	II	10	−62.5 to −57.3	8.4 to 15.0 (11.4)	−5.6 to −0.2 (−3.1)	147 to 430 (272.3)	0.81 to 2.74 (1.52)	0.71 to 0.92 (0.85)
BD-86a	Quartz	Mineralised vein (Qtz 1)	IIIa	9	−31.0 to −22.6	-	−9.0 to −0.2 (−3.1)	183 to 250 (197.6)	0.35 to 12.84 (4.61)	0.81 to 1.01 (0.90)
BD-85b	Quartz	Mineralised vein (Qtz 3)	IIIb	5	−27.5 to −24.1	-	−6.4 to −0.7 (−2.6)	-	2.40 to 9.70 (4.88)	-
GEF	Quartz	Red granite	I	6	−67.2 to −61.4	4.0 to 16.4 (9.3)	−8.1 to −1.2 (−3.6)	432 to 112 (329.7)	0.04 to 10.63 (3.65)	0.74 to 0.94 (0.87)

4.6.1. Fluid Inclusions Petrography

Analysed samples include quartz grains from the red granite, aplite, and mineralised veins (quartz 1 and quartz 3; [10]). Four types of fluid inclusions (type I, type II, types IIIa and IIIb) are identified based on their phase proportions at room temperature, according to the criteria of Roedder [55] and phase transitions during microthermometric measurements ([57]; Figures 15 and 16):

(i) Type I (H_2O-CO_2-NaCl) fluid inclusions are dominantly subhedral, isolated, and elongated in the direction of growth, demonstrating that they are primary in origin (Figure 15A). They are two-phase, liquid–vapor (liquid H_2O + vapor CO_2), ranging in size from 2 to 6 μm. They were observed only in the granite sample;

(ii) Type II (H_2O-CO_2-NaCl) fluid inclusions contain one vapor phase (vapor CO_2) and one liquid phase (liquid H_2O) or, possibly, two liquid phases (liquid H_2O + liquid CO_2). They vary in shape, from rounded, oval, triangular, to irregular, ranging in size from 3 to 18 μm and having variable vapor/liquid ratios (Figure 15B–E). They can be liquid-rich or vapor-rich as a function of their vapor/liquid proportion. Type II fluid inclusions are secondary in origin and are observed in the granite, aplite, and mineralised veins samples;

(iii) Type IIIa (H_2O-NaCl) fluid inclusions are rounded, occur as FIA in secondary trails, are 4–9 μm in size, and are two-phase (vapor H_2O + liquid H_2O; Figure 15A,F,G), while type IIIb (H_2O-NaCl) inclusions are monophase (liquid H_2O), 4–7 μm in size, and occur only as secondary trails in quartz 3 (Figure 15H) in association with gold-bearing minerals (e.g., pyrite 2b; [10]).

4.6.2. Microthermometry

Aqueous inclusions of type IIIa (H_2O-NaCl) were selected for first melting (T*fm*), ice melting (T*m*-ice), and total homogenisation (T*h*-tot) temperature measurements, while on aqueous–carbonic inclusions of types I and II (H_2O-CO_2-NaCl), measurements of the carbonic phase melting (T*m*-CO_2), CO_2 clathrate melting (T*m*-clath), partial homogenisation

of CO_2 (Th-CO_2) temperatures, and final Th-tot were performed. Microthermometric data of all fluid inclusion types are listed in Table 1.

CO$_2$-bearing inclusions—The Tm-CO_2 of types I and II (H_2O-CO_2-$NaCl$) inclusions ranges from −67.2 to −58.9 °C, and from −72 to −56 °C, respectively, temperatures slightly lower than the theoretical CO_2 triple point of −56.6 °C. This discrepancy indicates that other volatiles can be also present, such as SO_2 (as indicated by Raman spectroscopy, see Supplementary Material G—Figure S10—and Section 4.6). Tm-clath in the inclusions with CO_2 is between 4.5 °C and 14.7 °C (with an average value of 9.8 °C), below and above the invariant point of pure CO_2 clathrate (10 °C; [58]), thus also indicating the probable presence of other gases. The partial homogenisation of CO_2 in vapor CO_2, and less commonly in liquid CO_2, is between 17.6 and 38.2 °C (with an average value of 30.1 °C), far from the homogenisation temperature of −56.6 °C of pure CO_2. Ice melting in CO_2-bearing inclusions occurs between −11.6 and −0.2 °C (with an average value of −4.7 °C). Calculated salinities for type II inclusions range from 0.04 to 9.77 wt % NaCl eq. (with an average of 2.45 wt % NaCl eq.), whereas calculated densities from type II vary from 0.62 to 1.02 g/cm^3 (with an average value of 0.89 g/cm^3).

Aqueous fluid inclusions—Types IIIa and IIIb (H_2O-$NaCl$) have ice melting temperatures ranging from −9.0 to −0.2 °C and from −6.4 to −0.7 °C, respectively. The IIIa Th-tot varies from 183 to 249 °C (with an average value of 197 °C). The calculated salinities from types IIIa and IIIb range from 0.35 to 12.84 wt % NaCl eq. (with an average value of 4.61 wt % NaCl eq.) and from 2.4 to 9.7 wt % NaCl eq. (with an average value of 4.88 wt % NaCl eq.), respectively.

Diagrams showing Tfm vs. salinity and Th-tot vs. salinity plots have been reported (Figure 17A,B). The histograms of salinities and homogenisation temperatures are shown in Figure 18, and isochores have been traced in Figure 19. The fluid densities, salinities, and isochores were calculated using the CLATHRATE, FLUIDS, and ISOC software of Bakker [59]. For the isochore calculation of H_2O-$NaCl$ fluid inclusions, we used the equation of state proposed by [60,61]; and for isochore calculation of H_2O-CO_2-$NaCl$ fluid inclusions, we selected the equation of state proposed for any gas-mixture + NaCl [59,62,63]. In the pressure–temperature (P-T) diagram (Figure 19), we marked the temperatures obtained from the chlorite geothermometer (264 to 335 °C), thus bracketing the pressure of formation between 754 and 1585 bar for the gold mineralisation.

4.6.3. Laser Raman Spectroscopy

Gas and liquid phases of types II (H_2O-CO_2-$NaCl$) and IIIa (H_2O-$NaCl$) fluid inclusions were analysed by Laser Raman spectroscopy (Supplementary Material G: Figure S10). Spectra of type II inclusions show the presence of CO_2 and SO_2 peaks, representing the main volatiles in these inclusions (Supplementary Material E: Table S8). CO_2 peaks are observed at 1232 and 1355 cm^{-1}. In type IIIa fluid inclusions, the occurrence of SO_2 and H_2O is also suspected, but only CO_2 peaks have been identified (at 1233 cm^{-1}) (Supplementary Material G: Figure S10). No other gases were identified. These data are in coherence with the microthermometric data for CO_2-bearing inclusions (first melting temperatures at temperatures lower than −56.6 °C, triple point of pure CO_2), suggesting the presence of other volatiles (mainly SO_2). Type I (H_2O-CO_2-$NaCl$) fluid inclusions have not been analysed.

5. Discussion

5.1. Mineralisation and Alteration Paragenetic Sequence at the Passa Três Deposit

Based on field observations, and microscopic, QEMSCAN, SEM, and XRF analyses, two stages of alteration have been identified (Figures 6–10) that affected the main red granite facies of the Passa Três granite (Figure 2 and Figure S1—Supplementary Material A), in addition to late-stage argillic alteration detected in the fault gouge (Figure 11). These alteration styles have been named phengite–quartz–carbonate and sericite–carbonate–chlorite (Figures 7, 20 and 21). It has been established that the late magmatic stages in the Passa Três granite are marked by the formation of aplites, pegmatites, UST, and stockscheider [10]. Moreover, a spatial link between these features and the ore veins has

been used as an argument for the intrusion-related character of the deposit [10]. The two vein-related alteration styles are additional argument supporting this interpretation.
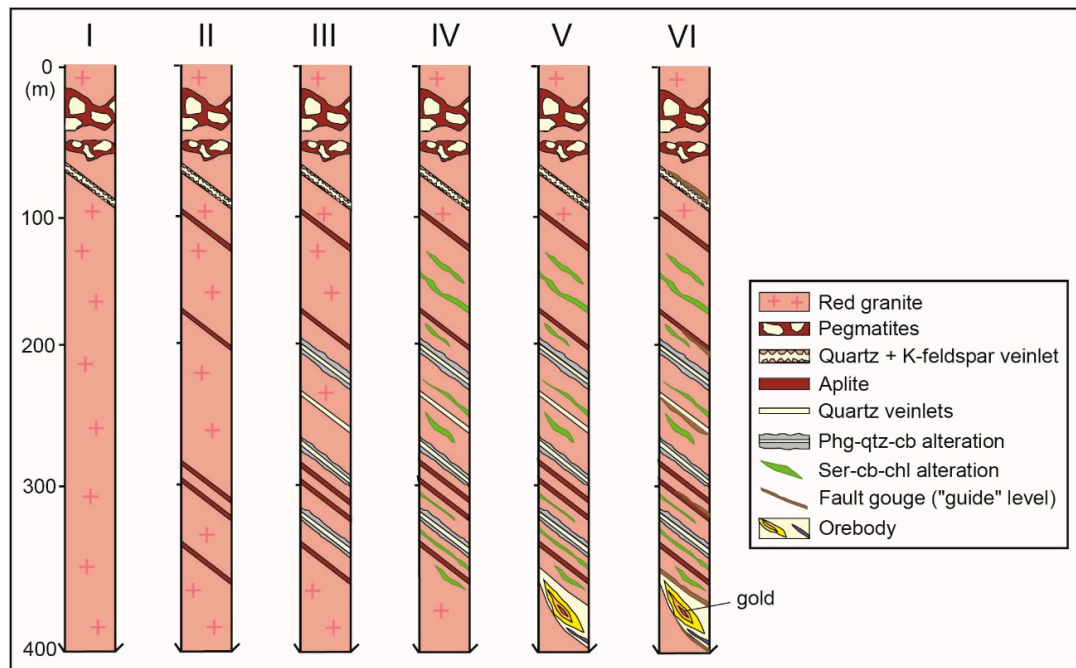

Figure 20. Schematic diagram of drill holes showing the evolutionary model of formation and distribution of the main alteration zones and mineralised veins. Different stages represent chronological order of events. Abbreviations: Cb—carbonate; Chl—chlorite; Phg—phengite; Qtz—quartz; Ser—sericite.
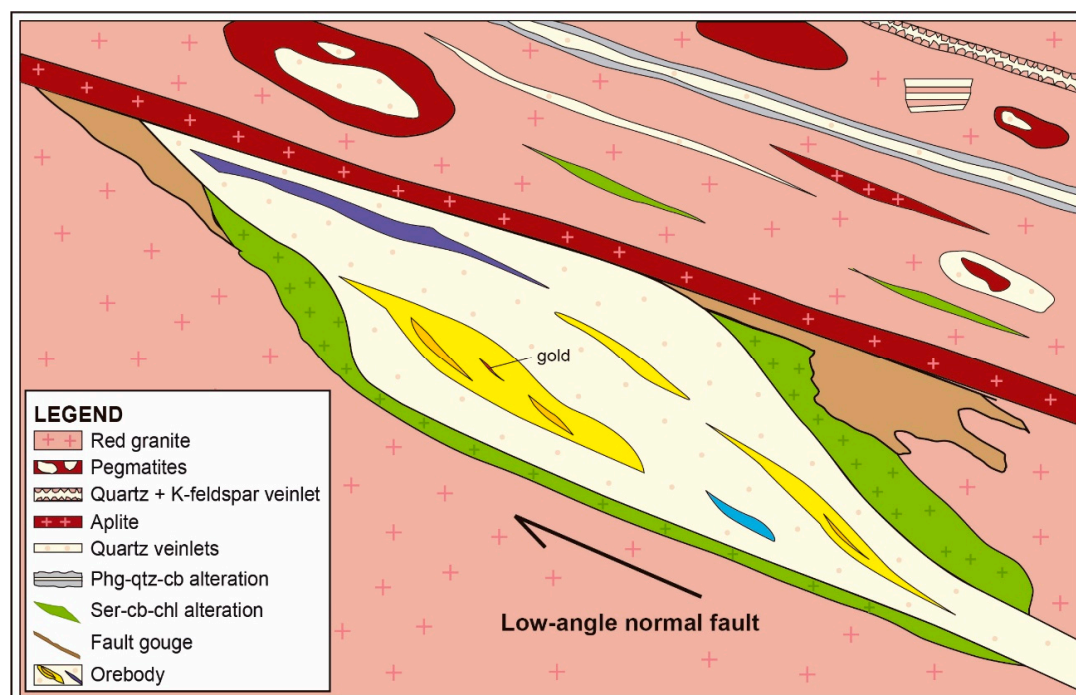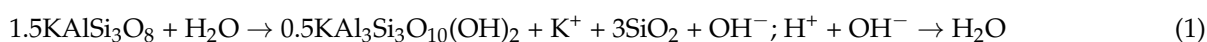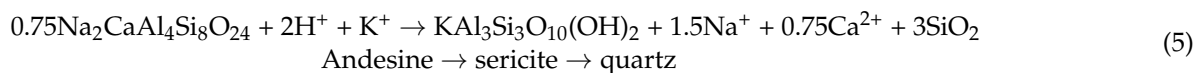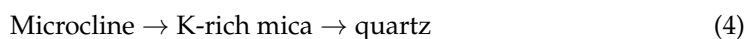

Figure 21. Schematic drawing showing the distribution of the different alteration styles related to the gold mineralisation, Passa Três granite, Barreiro zone. Abbreviations: Cb—carbonate; Chl—chlorite; Phg—phengite; Qtz—quartz; Ser—sericite. Not to scale.

A five-stage evolutionary model is proposed below (Figure 20). After the late magmatic stages (aplites and pegmatites) in the upper part of the Passa Três granite (Figure 20, stages I–II), the phengite–quartz–carbonate alteration developed mainly along barren quartz veins (Figure 20, stage III), which was followed by the formation of the sericite–carbonate–chlorite alteration halos (indicated by green colour in Figures 20 and 21) mainly around quartz veins either barren or mineralised (Figure 20, stages IV–V). During the formation of the main orebodies, normal fault activation created planes of brittle deformation and fracturing. This allowed the formation of the fault gouge in the main fault planes, which was recently replaced by clay minerals (argillic stage (fault gouge); Figure 20, stage VI). Gold mineralisation is associated dominantly with the sericite–carbonate–chlorite alteration. Late quartz/Fe-dolomite veinlets are also common and are related to a late reverse movement [10].

According to Pirajno [64], muscovite–quartz alteration is usually associated with the production of H^+ ions, involving the destabilisation and the destruction of feldspar and biotite to form a quartz + muscovite assemblage. This process occurs by the hydrolytic decomposition of feldspar according to the following reaction:

$$1.5KAlSi_3O_8 + H_2O \rightarrow 0.5KAl_3Si_3O_{10}(OH)_2 + K^+ + 3SiO_2 + OH^-; H^+ + OH^- \rightarrow H_2O \tag{1}$$

$$\text{K-feldspar + water} \rightarrow \text{K-rich mica + quartz} \tag{2}$$

Subsequent to this earlier alteration, sericite can occur by an increase in H^+ activity [64]. Sericite is essentially formed by the destabilisation of feldspars in the presence of H^+, OH^-, K, and S, forming quartz, white mica, pyrite, and some chalcopyrite. During this process, Na, Mg, Ti, Fe, and K are leached out and transferred to the solution [64]. Then, sericite may form by the following reactions:

$$3KAlSi_3O_8 + 2H^+ \rightarrow KAl_3Si_3O_{10}(OH)_2 + 2K^+ + 6SiO_2 \tag{3}$$

$$\text{Microcline} \rightarrow \text{K-rich mica} \rightarrow \text{quartz} \tag{4}$$

$$0.75Na_2CaAl_4Si_8O_{24} + 2H^+ + K^+ \rightarrow KAl_3Si_3O_{10}(OH)_2 + 1.5Na^+ + 0.75Ca^{2+} + 3SiO_2$$
$$\text{Andesine} \rightarrow \text{sericite} \rightarrow \text{quartz} \tag{5}$$

This alteration could be produced by hot fluid percolation through an existing fracture network and/or discrete micro-fractures, or possibly resulting from fluid circulation along grain boundaries, whose process was also considered by Piekarz [15] for the deposit. Similar narrow alteration halos around barren and mineralised veins were also observed in other deposits, such as Emerald Lake (quartz + muscovite + carbonate [1]) and Dublin Gulch (quartz + K-feldspar + albite + muscovite + carbonate + disseminated sulphide [65]) deposits. The alteration halos at the Passa Três deposit have also been observed by Piekarz [15] and attributed to temperatures from 275 to 390 °C, which is in accordance with entrapment conditions obtained by chlorite geothermometry in this study.

The presence of carbonate alteration, mainly ankerite and calcite, is common in syenite-associated and orogenic gold deposits; however, according to [66], these minerals occur in association with K-feldspar, albite, hematite, magnetite, and biotite, especially in syenite-related deposits, where albite and K-feldspar alterations are commonly well developed. This is not the case in the Passa Três deposit, where the occurrence of discrete alteration halos (from 0.5 to 3.0 cm-wide) around gold-bearing quartz veins is frequently considered as a characteristic for intrusion-related gold systems [1,9,67]. Regarding the predominance of sericite ± pyrite ± carbonate assemblage in the Passa Três deposit and the link with distal sericite–carbonate–chlorite alteration, we demonstrate that the studied deposit shares characteristics with mineralisation styles attributed to intrusion-related gold deposits.

5.2. Ore Fluid Composition

Based on petrographic observations, types II and III fluid inclusions were associated with the gold mineralisation stage, whereas type I was only observed in the magmatic quartz. More precisely, types IIIa and IIIb are associated to quartz 3, in paragenesis with the gold-bearing minerals. Based on the microthermometric data, it is shown that the ore fluid belongs to a medium- to low-temperature, moderate- to low-salinity, H_2O-$NaCl$-CO_2 fluid system (Figures 17 and 18).

During stages I to III, the salinities range between 0 and 4 wt % NaCl eq., with some inclusions showing higher salinities ranging from 9 to 12 wt % NaCl eq. (Figure 18A). Homogenisation temperatures of type II fluid inclusions range from 420 to 140 °C, whereas they range from 250 to 180 °C for type IIIa inclusions (Figure 18B).

The fluid inclusion data acquired during this study indicate a magmatic fluid system with primary inclusions of H_2O-$NaCl$-CO_2 in the magmatic quartz (type I), which were also dominant during the first stage of formation of the mineralised veins (type II, stage 2a) (see Section 4.1.2 for definition of the mineralisation stages and [10] for details). During stage 2b (type III fluid inclusions), where gold occurs in its native form with chalcopyrite and aikinite, the fluid has a H_2O-$NaCl$ composition and lower temperatures. Therefore, mineralising fluid during stages 1 and 2a belongs to the H_2O-CO_2-$NaCl$ system (with moderate temperature, enrichment of CO_2, and medium- to low salinity), and during stage 2b, the fluids have a H_2O-$NaCl$ composition, showing lower temperatures, low salinity, and no CO_2 in the late stages of mineralisation (as also observed in the Sanshandao deposit, China [68]). This interpretation is consistent with the work of Piekarz [15], who suggested that the fluids responsible for gold deposition can be represented by aqueous (5 to 9 mol % CO_2) and low-salinity (0.1 to 7.0 wt % NaCl eq.) fluid inclusions. This fluid is dominant during the final brittle stages of the deformation, which are associated with gold deposition at temperatures from 264 to 335 °C and pressures between 754 and 1585 bars.

Our fluid inclusion data can be compared with those from the Yukon gold deposits (e.g., Fort Knox, Dublin Gulch, Scheelite Dome, and Clear Creek), which formed from low- to moderate salinity ($\leq$12 wt % NaCl eq.) aqua-carbonic fluids at temperatures of 290 to 380 °C and with high CO_2 content (5–14%) [9,69]. Pressures from 1 to 2 kbar or 3.5 to 7.0 km depth were also estimated for these deposits [69].

5.3. Sources of Ore-Forming Fluids

The $\delta^{34}S$ isotopic composition of pyrite from the Barreiro zone gold veins has a narrow range from -2.1 to 4.3‰, indicating the magmatic origin of sulphur [3,70,71]. This suggests that the sulphur in the Passa Três deposit was most likely derived from a magmatic source, as already discussed by Picanço [16] (Supplementary Material F, Table S9).

The close association of the orebodies with features indicating magmatic–hydrothermal transition processes (as shown by [10]) and the H_2O-CO_2-$NaCl$ mineralising fluid composition, combined with $\delta^{34}S$ isotope data, are solid arguments indicating that ore-forming fluids at the Passa Três deposit had a dominantly magmatic origin [68,70,72].

5.4. Ore-Forming Processes

The formation of magmatic–hydrothermal ore deposits results from the combination of factors, such as the formation of a fractionated upper crustal magma chamber, the exsolution of aqueous fluids into a confined volume, vapor-brine immiscibility, magma mixing, fluid cooling and precipitation of ore minerals [9,64,70,72,73]. The orebodies in the Passa Três granite deposit (Barreiro zone) were emplaced within pull-apart structures [10,17] located close to the cupola area of a granitic pluton, as indicated by as the abundance of UST, stockscheider, and other magmatic–hydrothermal transition features, as described by [10]. The orebodies emplacement in this context shows that the mineralisation is formed in the late stages of the intrusion, thus disagreeing with the assumption of post-granite formation of the mineralisation, as proposed by [19], who considered a shear zone deposit, and [16]. In the same way, orogenic deposits form under compressional or transpressional tectonic

setting [74,75]; therefore, they are not compatible with the extensional setting at the Passa Três deposit, which is represented by orebodies hosted and controlled by extensional pull-aparts [10].

Fluid inclusion composition changes from the primary fluid inclusions hosted by magmatic quartz in the granite (type I) to the first (type II?) and the third mineralisation stages (type III). Such an evolution can be explained by various processes, such as fluid immiscibility and/or fluid–rock interaction [73,76,77]. Since our data show that alteration is weak and only expressed by discrete halos around the main orebodies, we favour the occurrence of fluid immiscibility, although we may not exclude fluid–rock interaction processes. During the main mineralisation stage, fluid inclusions are dominated by H_2O-NaCl-CO_2 composition (first and second stages), which is followed by a H_2O-NaCl composition (third stage). In some samples, the coexisting two-phase liquid-rich and vapor-rich fluid inclusions have variable Th-tot (Figure 18B) and homogenise to the liquid or vapour phase, suggesting that phase separation has occurred [78,79]. As in this study, the fluid inclusions analysed by microthermometry do not have evidence of post-entrapment modifications; these variations can be produced by unmixing from a parental homogeneous fluid (or, possibly, by the mixing of two different temperatures fluids; e.g., magmatic high temperature and meteoric low temperature) [80]. This can explain the large range of salinities, Th-tot temperatures, different vapor/liquid ratios, volatile constituents, and densities observed for type II inclusions (Figures 17 and 18; Table 1). In this case, unmixing can be related to the progressive decompression and the generation of "steam" [73,76,77]. In our study, the isochore diagram (Figure 19) shows that the isochores of type II fluid inclusions overlap with the isochores of types I and IIIa fluid inclusions, which are also entrapped probably at conditions, which could be explained by the fault-valve model [80–83] also considered for the Morro do Ouro gold deposit [80].

Indeed, considering the structural position of the gold mineralisation in the Passa Três deposit, its fluid inclusion characteristics and specific location (i.e., limited to the cupola zone—considered the whole outcropping length of the intrusion, 100 to 200 m below the carapace zone of the pluton, and probably immediately above the zone of volatile saturation [72]), we assume that decompression related to fault–valve processes in an extensional context could have occurred [80–83]. In this scenario, a sudden decrease from lithostatic to hydrostatic pressure could induce the escape of a steam-dominated fluid as previously described, close to the brittle–ductile transition and thus at a depth of 2 to 3 km, similarly to porphyry-type deposits [73]. However, disseminated ore was not observed throughout the underground mine of the Passa Três deposit as also related by the mine staff. In this case, the deposit also differs from porphyry-type and syenite-associated gold deposits [66,84], which share a disseminated ore style. Nevertheless, the absence of stockwork in intrusion-hosted deposits is frequently associated with a deeper level of emplacement (5–9 km [1]), and thus, stronger confining pressure can prevent rapid fluid exsolution and explosive pressure release. Indeed, in the latter case and also in the case of the Passa Três deposit, the structural context is the main parameter that controlled the orebodies geometry [67,73].

Finally, the observed succession in time and space from deformation features in relation with magmatic conditions (submagmatic fractures filled by quartz) to those related to ductile-brittle conditions (e.g., undulose quartz, pull-apart opening, sulphide fracturing, and gold precipitation [10]) agrees with a sequence of continuous and progressive events that resulted in the formation of the Passa Três gold deposit.

6. Conclusions

The mineralogical and fluid inclusion study of the Passa Três gold deposit samples allow the following conclusions:

- In the Passa Três granite, there are two alteration events that affected the red granite: (i) A phengite–quartz–carbonate alteration, related to barren quartz veins (during

magmatic–hydrothermal transition); and (ii) a sericite–carbonate–chlorite alteration, weakly developed but associated with the main ore-forming stage (hydrothermal stage).

- The δ^{34}S values of pyrite from the Passa Três deposit are indicative of the magmatic origin of the sulphur in the system.
- Petrographic observations and microthermometric data show that fluid inclusions in the Passa Três deposit have a H_2O-CO_2-NaCl composition and were trapped at moderate to high temperatures (400 to 100 °C) and have low to moderate salinities (0.04 to 12.84 wt % NaCl eq.).
- Mineralising fluid is derived, at least in part, from magmatic fluid during the late magmatic stage (aplites, pegmatites, UST, stockscheider textures) that evolved to early hydrothermal fluids (early hydrothermal veins with K-feldspar border and barren quartz veins) and, finally, formed the mineralised quartz veins. Processes such as fluid decompression, immiscibility, and cooling are also considered as important for ore deposition, in addition to the structural setting that dominantly controlled the deposit formation.

Field evidence, structural characteristics, mineralising fluid physico-chemical parameters, and alteration styles all suggest that the Passa Três gold deposit shares characteristics of intrusion-related gold systems, having an intimate relationship with the Passa Três granite and thus can be classified as a granite-hosted deposit. Thus, the definition of this specific intrusion-related/hosted type of mineralization is a fundamental result that can be applied to the discovery of new deposits close to our studied area where numerous similar intrusions exist but also everywhere in the world.

Supplementary Materials: The following supporting information can be downloaded at: https://www.mdpi.com/article/10.3390/min12040407/s1, Files Supplementary Materials A, B, C, D [85,86] E, F and G.

References

1. Baker, T.; Lang, J. Fluid inclusion characteristics of intrusion-related gold mineralization, Tombstone—Tungsten magmatic belt, Yukon Territory, Canada. *Miner. Depos.* **2001**, *36*, 563–582. [CrossRef]
2. Cepedal, A.; Fuertes-Fuente, M.; Martín-Izard, A.; García-Neto, J.; Boirin, M.C. An intrusion-related gold deposit (IRGD) in the NW of Spain, the Linares deposit: Igneous rocks, veins and related alterations, ore features and fluids involved. *J. Geochem. Explor.* **2013**, *124*, 101–126. [CrossRef]
3. Assunção, R.F.S.; Klein, E.L. The Moreira Gomes deposit of the Caiú-Caiú goldfield: Fluid inclusions and stable isotope constraints and implications for the genesis of granite-hosted gold mineralization in the Tapajós Gold Province, Brazil. *J. S. Am. Earth Sci.* **2014**, *49*, 85–105. [CrossRef]
4. Gloaguen, E.; Branquet, Y.; Chauvet, A.; Bouchot, V.; Barbanson, L.; Vigneresse, J.J. Tracing the magmatic/hydrothermal transition in regional low-strain zones: The role of magma dynamics in strain localization at pluton roof, implications for intrusion-related gold deposits. *J. Struct. Geol.* **2014**, *58*, 108–121. [CrossRef]

5. Marcoux, E.; Nerci, K.; Branquet, Y.; Ramboz, C.; Ruffet, G.; Peucat, J.J.; Stevenson, R.; Jébrak, M. Late-Hercynian intrusion-related gold deposits: An integrated model on the Tighza polymetallic district, central Morocco. *J. Afr. Earth Sci.* **2015**, *107*, 65–88. [CrossRef]
6. Hart, C.; Goldfarb, R. Distinguishing Intrusion-Related from Orogenic Gold Systems. In Proceedings of the Scientific Conference on Minerals, Auckland, New Zealand, 13–16 November 2005; Available online: https://www.researchgate.net/publication/2287 62286_Distinguishing_intrusion-related_from_orogenic_gold_systems (accessed on 1 January 2015).
7. Thompson, J.F.H.; Sillitoe, R.H.; Baker, T.; Lang, J.R.; Mortensen, J.K. Intrusion-related gold deposits associated with tungsten-tin provinces. *Miner. Depos.* **1999**, *34*, 323–334. [CrossRef]
8. Lang, J.R.; Baker, T. Intrusion-related gold systems: The present level of understanding. *Miner. Depos.* **2001**, *36*, 477–489. [CrossRef]
9. Hart, C.J.R. Reduced intrusion-related gold systems. In *Mineral Deposits of Canada: A Synthesis of Major Deposit Types, District Metallogeny, the Evolution of Geological Provinces, and Exploration Methods*; Goodfellow, W.D., Ed.; Special Publication n. 5; Geological Association of Canada: St. John, NL, Canada, 2007; pp. 95–112.
10. Dressel, B.C.; Chauvet, A.; Trzaskos, B.; Biondi, J.C.; Bruguier, O.; Monié, P.; Villanova, S.N.; Newton, J.B. The Passa Três lode gold deposit (Paraná State, Brazil): An example of structurally-controlled mineralisation formed during magmatic-hydrothermal transition and hosted within granite. *Ore Geol. Rev.* **2018**, *102*, 701–727. [CrossRef]
11. Soares, P.C.; Góis, J.R. Geologia do Granito Passa Três (Paraná) e suas mineralizações auríferas. In *3rd Simpósio Sul Brasileiro de Geologia (Atas . . .)*; Brazilian Society of Geology (Sociedade Brasileira de Geologia): Curitiba, Brazil, 1987; Volume 2, p. 497.
12. Chiodi Filho, C.; Santos, J.F.; Soares, P.C.; Moretzshon, J.S. Estudo ETR para caracterização e avaliação metalogenética de granitóides no escudo paranaense. In *2nd Congresso Brasileiro de Geoquímica (Anais . . .)*; Brazilian Society of Geology (Sociedade Brasileira de Geologia): Rio de Janeiro, Brazil, 1989; Volume 1, pp. 487–498.
13. Piekarz, G.F.; Schrank, A.; Choudhuri, A.; Figueiredo, B.; Xavier, R. A porphyry-type gold deposit in the Passa Três Granite, South Brazil. In *Brazil Gold 91: The Economics Geology Geochemistry and Genesis of Gold Deposit*; Ladeira, E.A., Ed.; Balkema: Rotterdam, The Netherlands, 1991; pp. 541–546.
14. Riedel, W. Zur Mechanick Geologischer Brucherscheinungen. *Cent. Mineral. Geol. Paläontologie B* **1929**, *8*, 354–368.
15. Piekarz, G.F. O Granito Passa Três—PR e as Mineralizações Auríferas Associadas. Master's Thesis, Universidade Estadual de Campinas (Instituto de Geociências), Campinas, Brazil, 1992; 221p.
16. Picanço, J.L. Composição Isotópica e Processos Hidrotermais Associados aos Veios Auríferos do Maciço Granítico Passa Três, Campo Largo, PR. Ph.D. Thesis, Universidade de São Paulo (Instituto de Geociências), São Paulo, Brazil, 2000; 175p. [CrossRef]
17. Dressel, B.C. Análise Estrutural, Petrológica e Metalogenética da Mineralização Aurífera Neorpoterozoica do Granito Passa Três (Campo Largo—PR)—Implicações Sobre as Relações Granito/Mineralização. Analyse Structurale, Pétrologique et Métallogénique de la Minéralisation Aurifère du Granite Passa Três (Campo Largo—PR, Sud du Brésil)—Implications sur les Relations Granite/Minéralisation. Ph.D. Thesis, Universidade Federal do Paraná, Curitiba, Brazil, Université Montpellier (Géosciences Montpellier), Montpellier, France, 2018; 193p. Available online: https://hdl.handle.net/1884/59959 (accessed on 18 December 2018).
18. Turini Neto, G. Estudos Geoquímicos da Mineralização Aurífera do Granito Passa Três—PR. Master's Thesis, Universidade de São Paulo (Instituto de Geociências), São Paulo, Brazil, 2012; 47p.
19. Sacoman, D. Microestruturas em Veios de Quartzo-Sulfetados Mineralizados em Ouro, Granito Passa Três, Campo Largo—Paraná. Master's Thesis, Universidade Federal do Paraná, Curitiba, Brazil, 2015; 58p.
20. Pontes, J.B. Geologia e potencialidades econômicas da formação Água Clara (PR). In *32nd Congresso Brasileiro de Geologia (Anais . . .)*; Brazilian Society of Geology (Sociedade Brasileira de Geologia): Salvador, Brazil, 1982; Volume 3, pp. 1002–1016.
21. Biondi, J.C. Typological and quantitative classification of mineral deposits with gold. In *Brazil Gold 91: The Economics Geology Geochemistry and Genesis of Gold Deposit*; Ladeira, E.A., Ed.; Balkema: Rotterdam, The Netherlands, 1991; pp. 523–534.
22. Mesquita, M.J.; Marczyski, E.S.; Vasconcelos, E.M.G.; Picanço, J.; Salamuni, E. Alteração hidrotermal precoce das mineralizações de Au tipo veio da Mina do Morro, Campo Largo, PR. In *41st Congresso Brasileiro de Geologia (Anais . . .)*; Brazilian Society of Geology (Sociedade Brasileira de Geologia): João Pessoa, Brazil, 2002; Volume 1, p. 216.
23. Heilbron, M.; Pedrosa-Soares, A.C.; Campos Neto, M.d.C.; da Silva, L.C.; Trouw, R.A.J.; Janasi, V.A. Província Mantiqueira. In *Geologia do Continente Sul-Americano: Evolução da Obra de Fernando Flávio Marques de Almeida*; Mantesso-Neto, V., Bartorelli, A., Carneiro, C.D.R., de Orgs Brito-Neves, B.B., Eds.; Deca: São Paulo, Brazil, 2004; pp. 203–234.
24. Fiori, A.P.; Fassbinder, E.; Góis, J.R.; Fumagalli, C.E. Compartimentação tectônica do Grupo Açungui a norte de Curitiba. In *3rd Simpósio Sul Brasileiro de Geologia (Atas . . .)*; Brazilian Society of Geology (Sociedade Brasileira de Geologia): Curitiba, Brazil, 1987; Volume 1, pp. 183–196.
25. Fiori, A.P. Tectônica e estratigrafia do Grupo Açungui, PR. *Bol. IG-USP Série Científica* **1992**, *23*, 55–74. [CrossRef]
26. Fiori, A.P. Evolução geológica da Bacia Açungui. *Bol. Parana. Geociências* **1994**, *42*, 7–27.
27. Fassbinder, E. A Unidade Água Clara No Contexto do Grupo Açungui: Um Modelo Transpressivo de Colisão Oblíqua No Neoproterozóico Paranaense. Ph.D. Thesis, Universidade de São Paulo (Instituto de Geociências), São Paulo, Brazil, 1996; 207p. [CrossRef]
28. Kaulfuss, G.A. Geocronologia dos Núcleos de Embasamento Setuva, Betara e Tigre, Norte de Curitiba-PR. Master's Thesis, Universidade de São Paulo (Instituto de Geociências), São Paulo, Brazil, 2001; 115p. [CrossRef]

29. Cury, L.F.; Kaulfuss, G.A.; Siga, O., Jr.; Basei, M.A.S.; Harara, O.M.; Sato, K. Idades U-Pb (Zircões) de 1.75 Ga em granitóides alcalinos deformados dos núcleos Betara e Tigre: Evidências de regimes extensionais do Estateriano na Faixa Apiaí. *Geol. USP Série Científica* **2002**, *2*, 95–108. [CrossRef]

30. Basei, M.A.S.; Brito Neves, B.B.; Siga, O., Jr.; Babinski, M.; Pimentel, M.M.; Tassinari, C.C.G.; Hollanda, M.H.B.; Nutman, A.; Cordani, U.G. Contribution of SHRIMP U–Pb zircon geochronology to unravelling the evolution of Brazilian Neoproterozoic fold belts. *Precambrian Res.* **2010**, *183*, 112–144. [CrossRef]

31. Campanha, G.A.C.; Sadowski, G.R. Tectonics of the southern portion of the Ribeira Belt (Apiaí Domain). *Precambrian Res.* **1999**, *98*, 31–51. [CrossRef]

32. Siga, O., Jr.; Basei, M.A.S.; Passarelli, C.R.; Sato, K.; Cury, L.F.; McReach, I. Lower and Upper Neoproterozoic magmatic records in Itaiacoca Belt (Paraná-Brazil): Zircon ages and lithostratigraphy studies. *Gondwana Res.* **2009**, *15*, 197–208. [CrossRef]

33. Fragoso Cesar, A.R.S.; Soares, P.C. As placas brasilianas do sul e sudeste da Plataforma Sul-Americana. In *4st Simpósio Nacional de Estudos Tectônicos (Atas . . .)*; Brazilian Society of Geology (Sociedade Brasileira de Geologia): Belo Horizonte, Brazil, 1993.

34. Campos Neto, M.C.; Figueiredo, M.C.H. The Rio Doce Orogeny, Southeastern Brazil. *J. S. Am. Earth. Sci.* **1995**, *8*, 143–162. [CrossRef]

35. Rogers, J.J.W.; Unrug, R.; Sultan, M. Tectonic assembly of Gondwana. *J. Geodyn.* **1995**, *19*, 1–34. [CrossRef]

36. Gimenez Filho, A.G.; Janasi, V.A.; Campanha, G.A.C.; Teixeira, W.; Trevizoli, L.E., Jr. U-Pb dating and Rb-Sr isotope geochemistry of the Eastern portion of the Três Córregos Batolith Ribeira Fold Belt, São Paulo, Brazil. *Rev. Bras. Geociências* **2000**, *30*, 45–50. [CrossRef]

37. Prazeres Filho, H.J. Litogeoquímica, Geocronologia (U-Pb) e Geologia Isotópica dos Complexos Graníticos Cunhaporanga e Três Córregos, Estado do Paraná. Master's Thesis, Universidade de São Paulo (Instituto de Geociências), São Paulo, Brazil, 2000; 180p. [CrossRef]

38. Janasi, V.A.; Leite, R.J.; Van Schmu, W.R. U-Pb chronostratigraphy of the granitic magmatism in the Agudos Grandes Batholith (west of São Paulo)—Implications for the evolution of the Ribeira Belt. *J. S. Am. Earth. Sci.* **2001**, *14*, 363–376. [CrossRef]

39. Prazeres Filho, H.J.; Basei, M.A.S.; Passarelli, C.R.; Harara, O.M.M.; Siga, O., Jr. U-Pb Zircon ages of post-orogenetic granitic magmatism in Apiaí Folded Belt (Paraná State, Southern Brazil): Petrological and geotectonic significance. In *4st South American Symposium on Isotope Geology (Short Papers)*; CBPM: Salvador, Brazil, 2003.

40. Prazeres Filho, H.J.; Harara, O.M.; Basei, M.A.S.; Passarelli, C.R.; Siga, O., Jr. Litogeoquímica, geocronologia U-Pb e geologia isotópica (Sr-Nd-Pb) das rochas graníticas dos batólitos Cunhaporanga e Três Córregos na porção sul do Cinturão Ribeira, Estado do Paraná. *Geol. USP Série Científica* **2003**, *3*, 51–70. [CrossRef]

41. Fiori, A.P. Aplicação do modelo de cisalhamento simples na análise da deformação dúctil de alguns granitos paranaenses. *Bol. Parana. Geociências* **1985**, *36*, 31–40.

42. Cury, L.F. Geocronologia e Litogeoquímica dos Stocks Graníticos da Porção Sudeste da Faixa Apiaí, Estado do Paraná. Master's Thesis, Universidade de São Paulo (Instituto de Geociências), São Paulo, Brazil, 2003; 125p. [CrossRef]

43. Faleiros, F.M. Evolução de Terrenos Tectono-Metamórficos da Serrania do Ribeira e Planalto Alto Turvo (SP, PR). Ph.D. Thesis, Universidade de São Paulo (Instituto de Geociências), São Paulo, Brazil, 2008; 318p. [CrossRef]

44. Wilson, S.A.; Ridley, W.I.; Koenig, A.E. Development of sulfide calibration standards for the laser ablation inductivelt-coupled plasma mass spectrometry technique. *J. Anal. At. Spectrom.* **2002**, *17*, 406–409. [CrossRef]

45. Pirrie, D.; Butcher, A.R.; Power, M.R.; Gottlieb, P.; Miller, G.L. Rapid Quantitative Mineral and Phase Analysis Using Automated Scanning Electron Microscopy (QEMSCAN); Potential Applications in Forensic Geoscience. In *Geological Society, London, Special Publication 232*; Geological Society: London, UK, 2004; pp. 123–136.

46. Nakano, S.; Akai, J.; Shimobayashi, N. Contrasting Fe-Ca distributions and related microtextures in syenite alkali feldspar from the Patagonian Andes, Chile. *Mineral Mag.* **2005**, *69*, 521–535. [CrossRef]

47. Putnis, A.; Hinrichs, R.; Putnis, C.V.; Golla-Schindler, U.; Collins, L.G. Hematite in porous red-clouded feldpars: Evidence of large-scale crustal fluid-rock interaction. *Lithos* **2007**, *95*, 10–18. [CrossRef]

48. Parsons, I.; Fitz Gerald, J.D.; Lee, M.R. Routine characterization and interpretation of complex alkali feldspar intergrowths. *Am. Min.* **2015**, *100*, 1277–1303. [CrossRef]

49. Crespo, J.; Holley, E.; Pfaff, K.; Guillen, M.; Huamani, R. Ore mineralogy, trace element geochemistry and geochronological constraints at the Mollehuaca and San Juan de Chorunga Au-Ag vein deposits in the Nazca-Ocoña metallogenic belt, Arequipa, Peru. Minerals. *Minerals* **2020**, *10*, 1112. [CrossRef]

50. Pokrovski, G.S.; Escoda, C.; Blanchard, M.; Testemale, D.; Hazeman, J.-L.; Gouy, S.; Kokh, M.A.; Boiron, M.-C.; de Parseval, F.; Aigouy, T.; et al. An arsenic-driven pump for invisible gold in hydrothermal systems. *Geochem. Perspect. Lett.* **2021**, *17*, 39–44. [CrossRef]

51. Reich, M.; Kesler, S.E.; Utsunomiya, S.; Palenik, C.S.; Chryssoulis, S.L.; Ewing, R.C. Solubility of gold in arsenian pyrite. *Geochim. Cosmocnim. Acta* **2005**, *69*, 2781–2796. [CrossRef]

52. Cathelineau, M.; Izquierdo, G.; Nieva, D. Thermobarometry of hydrothermal alteration in the Los Azufres geothermal system (Michoacan, Mexico): Significance of fluid-inclusion data. *Chem. Geol.* **1989**, *76*, 229–238. [CrossRef]

53. Deer, W.A.; Howie, R.A.; Zussman, J. *Minerais Constituintes das Rochas*, 4th ed.; Fundação Calouste Gulbenkian: Lisboa, Portugal, 2010; 727p.

54. MacLean, W.H. Mass change calculations in altered rock series. *Miner. Depos.* **1990**, *25*, 44–49. [CrossRef]

55. Roedder, E. *Fluid Inclusions (Reviews in Mineralogy, Volume 12)*; Mineralogical Society of America: Chantilly, WV, USA, 1984; 646p.

56. Goldstein, R.H.; Reynolds, T.J. Systematics of fluid inclusions in diagenetic minerals. In *Society for Sedimentary Geology, Society of Economic Paleontologists and Mineralogists, Short Course 31*; SEPM (Society for Sedimentary Geology): Tulsa, OK, USA, 1994; p. 199.

57. Diamond, L.W. Review of the systematics of CO_2–H_2O fluid inclusions. *Lithos* **2001**, *55*, 69–99. [CrossRef]

58. Hollister, L.S.; Burrus, R.C. Phase equilibria in fluid inclusions from Khatada Lake metamorphic complex. *Geochim. Cosmochim. Acta* **1976**, *40*, 163–175. [CrossRef]

59. Bakker, R.J. Package FLUIDS 1. Computer programs for analysis of fluid inclusion data and for modelling bulk fluid properties. *Chem. Geol.* **2003**, *194*, 3–23. [CrossRef]

60. Knight, C.L.; Bodnar, R.J. Synthetic fluid inclusions: IX. Critical PVTX properties of $NaCl$-H_2O solutions. *Geochim. Cosmochim. Acta* **1989**, *53*, 3–8. [CrossRef]

61. Bodnar, R.J.; Vityk, M.O. Interpretation of microthermometric data for H_2O–$NaCl$ fluid inclusions. In *Fluid Inclusions in Minerals: Methods and Applications*; de Vivo, B., Frezzotti, M.L., Eds.; Short Course IMA: Pontignano-Siena, Italy, 1994; pp. 117–130.

62. Bowers, T.S.; Helgeson, H.C. Calculation of the thermodynamic and geochemical consequences of nonideal mixing in the system H_2O-CO_2-$NaCl$ on phase relations in geological systems: Equation of state for H_2O-CO_2-$NaCl$ fluids at high pressures and temperatures. *Geochim. Cosmochim. Acta* **1983**, *47*, 1247–1275. [CrossRef]

63. Bakker, R.J. Adaptation of the Bowers and Helgeson 1983 equation of state to the H_2O-CO_2-CH_4-N_2-$NaCl$ system. *Chem. Geol.* **1999**, *154*, 225–236. [CrossRef]

64. Pirajno, F. *Hydrothermal Processes and Mineral Systems*; Springer & Geological Survey of Western Australia: Dordrecht, Australia, 2009; 1250p.

65. Maloof, T.L.; Baker, T.; Thompson, J.F.H. The Dublin Gulch intrusion-hosted gold deposit, Tombstone plutonic suite, Yukon Territory, Canada. *Miner. Depos.* **2001**, *36*, 583–593. [CrossRef]

66. Robert, F. Syenite-associated disseminated gold deposits in the Abitibi greenstone belt, Canada. *Miner. Depos.* **2001**, *36*, 503–516. [CrossRef]

67. Stephens, J.L.; Mair, J.L.; Oliver, N.H.S.; Hart, C.J.R.; Baker, T. Structural and mechanical controls on intrusion-related deposits of the Tombstone Gold Belt, Yukon, Canada, with comparisons to other vein-hosted ore-deposit types. *J. Struct. Geol.* **2004**, *26*, 1025–1041. [CrossRef]

68. Wen, B.J.; Fan, H.R.; Hu, F.F.; Liu, X.; Yang, K.F.; Sun, Z.F. Fluid evolution and ore genesis of the giant Sanshandao gold deposit, Jiaodong gold province, China: Constrains from geology, fluid inclusions and H–O–S–He–Ar isotopic compositions. *J. Geochem. Explor.* **2016**, *171*, 96–112. [CrossRef]

69. Goldfarb, R.J.; Marsh, E.E.; Hart, C.J.R.; Mair, J.L.; Miller, M.L.; Johnson, C. Geology and Origin of Epigenetic Lode Gold Deposits, Tintina Gold Province, Alaska and Yukon. In *Recent U.S. Geological Survey Studies in the Tintina Gold Province, Alaska, United States, and Yukon, Canada—Results of a 5-Year Project*; Scientific Investigations Report; Gough, L.P., Day, W.C., Eds.; U.S. Geological Survey: Reston, VA, USA, 2007. [CrossRef]

70. Hedenquist, J.W.; Lowenstern, J.B. The role of magmas in the formation of hydrothermal ore deposits. *Nature* **1994**, *370*, 519–527. [CrossRef]

71. Biondi, J.C. *Processos Metalogenéticos e os Depósitos Minerais Brasileiros*, 2nd ed.; Oficina de Textos: São Paulo, Brazil, 2015; 552p.

72. Audétat, A.; Pettke, T.; Heinrich, C.A.; Bodnar, R.J. The Composition of Magmatic-Hydrothermal Fluids in Barren and Mineralized Intrusions. *Econ. Geol.* **2008**, *103*, 877–908. [CrossRef]

73. Fournier, R.O. Hydrothermal processes related to movement of fluid from plastic into brittle rock in the magmatic-epithermal environment. *Econ. Geol.* **1999**, *94*, 1193–1211. [CrossRef]

74. Groves, D.I.; Goldfarb, R.J.; Gebre-Mariam, M.; Hagemann, S.G.; Robert, F. Orogenic gold deposits: A proposed classification in the context of their crustal distribution and relationship to other gold deposit types. *Ore Geol. Rev.* **1998**, *13*, 7–27. [CrossRef]

75. Goldfarb, R.J.; Baker, T.; Dubé, B.; Groves, D.I.; Hart, C.J.R.; Gosselin, P. Distribution, character, and genesis of gold deposits in metamorphic terrain. In *One Hundredth Anniversary Volume*; Hedenquist, J.W., Thompson, J.F.H., Goldfarb, R.J., Richards, J.P., Eds.; Society of Economic Geologists: McLean, WV, USA, 2005. [CrossRef]

76. Wilkinson, J.J. Fluid inclusions in hydrothermal ore deposits. *Lithos* **2001**, *55*, 229–272. [CrossRef]

77. Hurai, V.; Huraiová, M.; Slobodni'k, M.; Thomas, R. *Geofluids Developments in Microthermometry, Spectroscopy, Thermodynamics, and Stable Isotopes*, 1st ed.; Elsevier: Amsterdam, The Netherlands, 2015; 504p.

78. Fan, H.R.; Hu, F.F.; Yang, J.H.; Shen, K.; Zhai, M.G. Fluid inclusion and large-scale gold metallogeny during Meozoic tectonic transition in the eastern Shandong province. *Acta Petrol. Sin.* **2005**, *21*, 1317.

79. Deng, J.; Liu, X.; Wang, Q.; Pan, R. Origin of the Jiaodong-type Xinli gold deposit, Jiaodong Peninsula, China: Constraints from fluid inclusion and C–D–O–S–Sr isotope compositions. *Ore Geol. Rev.* **2015**, *65*, 674–686. [CrossRef]

80. Faleiros, A.M.; Campanha, G.A.C.; Faleiros, F.M.; Bello, R.M.S. Fluid regimes, fault-valve behavior and formation of gold-quartz veins—The Morro do Ouro Mine, Ribeira Belt, Brazil. *Ore Geol. Rev.* **2014**, *56*, 442–456. [CrossRef]

81. Boullier, A.M.; Robert, F. Palaeoseismic events recorded in Archaean gold-quartz vein networks, Val d'Or, Abitibi, Quebec, Canada. *J. Struct. Geol.* **1992**, *14*, 161–179. [CrossRef]

82. Sibson, R.H. Fluid involvement in normal faulting. *J. Geodyn.* **2000**, *29*, 469–499. [CrossRef]

83. Famin, V.; Hébert, R.; Philippot, P.; Jolivet, L. Ion probe and fluid inclusion evidence for co-seismic fluid infiltration in a crustal detachment. *Contrib. Mineral. Petrol.* **2005**, *150*, 354–367. [CrossRef]

84. Bigot, L.; Jébrak, M. Gold mineralization at the syenite-hosted Beattie gold deposit, Duparquet, Neoarchean Abitibi Belt, Canada. *Econ. Geol.* **2015**, *110*, 315–335. [CrossRef]

85. Bailey, S.W. Chlorites: Structures and crystal chemistry. *Rev. Mineral.* **1988**, *19*, 347–403.

86. Beaufort, D. Etude Pétrographique des Altérations Hydrothermales Superposées Dans le Porphyre Cuprifère de Sibert (Rhône): Influence des Microsystèmes Géochimiques dans la Différenciation des Micas Blancs et des Phases Trioctaédriques. Ph.D. Thesis, Faculté des Sciences, Poitiers, France, 1981; 147p.